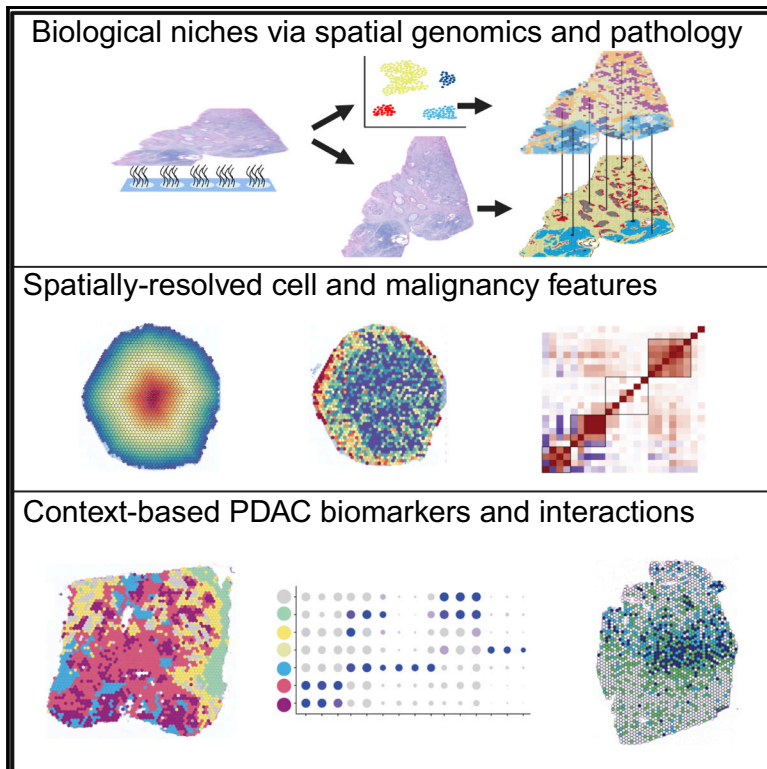


Assessment of spatial transcriptomics for oncology discovery

Graphical abstract



Authors

Anna Lyubetskaya, Brian Rabe, Andrew Fisher, ..., Kenzie MacIsaac, Benjamin J. Chen, Eugene Drokhlyansky

Correspondence

eugene.drokhlyansky@bms.com

In brief

Lyubetskaya et al. undertake an assessment of spatial transcriptomics methods across normal and tumor tissue to help inform the selection of effective approaches for profiling human tumors. They demonstrate the potential of spatial transcriptomics for probing the biology of pancreatic cancer and future oncology drug discovery.

Highlights

- 80,024 spots profiled across diverse tissue types using spatial transcriptomics
- Pathology enhancement of transcriptional data captures biological niches
- Cell-type and depth features are distinctly contextualized in syngeneic tumors
- Tumor-specific biomarkers and interactions are identified in donor PDAC



Resource

Assessment of spatial transcriptomics for oncology discovery

Anna Lyubetskaya,^{1,4} Brian Rabe,^{1,4} Andrew Fisher,¹ Anne Lewin,¹ Isaac Neuhaus,² Constance Brett,³ Todd Brett,³ Ethel Pereira,¹ Ryan Golhar,² Sami Kebede,¹ Alba Font-Tello,¹ Kathy Mosure,¹ Nicholas Van Wittenbergh,¹ Konstantinos J. Mavrikis,¹ Kenzie MacIsaac,¹ Benjamin J. Chen,¹ and Eugene Drokhlyansky^{1,5,*}

¹Research and Early Development, Bristol Myers Squibb Company, 100 Binney Street, Cambridge, MA 02142, USA

²Research and Early Development, Bristol Myers Squibb Company, Route 206 & Province Line Road, Princeton, NJ 08543, USA

³Aggregate Genius, Inc., 560 Fulford-Ganges Road, Salt Spring Island, BC V8K 2K1, Canada

⁴These authors contributed equally

⁵Lead contact

*Correspondence: eugene.drokhlyansky@bms.com

<https://doi.org/10.1016/j.crmeth.2022.100340>

MOTIVATION Tumor heterogeneity is a major challenge for oncology drug discovery and development. Identifying new targets and appropriate model systems requires an accurate spatial and molecular disease taxonomy. Advances in spatial genomics hold promise for broad characterization of tumor structure, contextualization of established biomarkers, and *de novo* identification of interactions. We sought to appraise the utility of spatial genomics technologies for oncology drug discovery.

SUMMARY

Tumor heterogeneity is a major challenge for oncology drug discovery and development. Understanding of the spatial tumor landscape is key to identifying new targets and impactful model systems. Here, we test the utility of spatial transcriptomics (ST) for oncology discovery by profiling 40 tissue sections and 80,024 capture spots across a diverse set of tissue types, sample formats, and RNA capture chemistries. We verify the accuracy and fidelity of ST by leveraging matched pathology analysis, which provides a ground truth for tissue section composition. We then use spatial data to demonstrate the capture of key tumor depth features, identifying hypoxia, necrosis, vasculature, and extracellular matrix variation. We also leverage spatial context to identify relative cell-type locations showing the anti-correlation of tumor and immune cells in syngeneic cancer models. Lastly, we demonstrate target identification approaches in clinical pancreatic adenocarcinoma samples, highlighting tumor intrinsic biomarkers and paracrine signaling.

INTRODUCTION

Tumors exist in a complex microenvironment where malignant and non-malignant cells interact in distinct compartments, including the tumor parenchyma (i.e., tumor cells), stroma (e.g., fibroblasts and vasculature), and immune system (e.g., adaptive and innate immune cells).^{1–4} Interactions can occur within these compartments, such as commensal dynamics between heterogeneous tumor clones,⁵ or across compartments such as immune suppression by tumor cells.⁶ This extensive cellular heterogeneity and signaling complexity drives cancer evolution and therapy response and resistance.

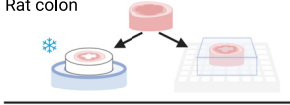

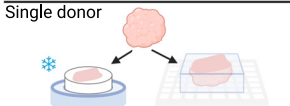
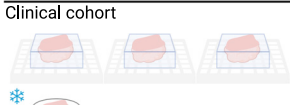
Tumor heterogeneity is a major challenge for oncology drug discovery and development^{3,4,7} and reductionist model systems (e.g., cultured cells and mouse models) may not recapitulate human tumor complexity. Identifying new targets and appropriate model systems requires an accurate spatial and molecular tax-

onomy of the tumor landscape.⁸ Recent advances in spatial genomics^{9–17} hold promise for broad characterization of tumor tissue structure, spatial contextualization of established biomarkers, and *de novo* identification of spatial interactions by preserving the localization of tissue transcriptomes within their native architecture.^{18,19} We undertook a systematic study to appraise the utility of spatial genomics technologies (i.e., 10x Visium; herein referred to as spatial transcriptomics [ST]) for oncology, specifically focusing on drug discovery applications.

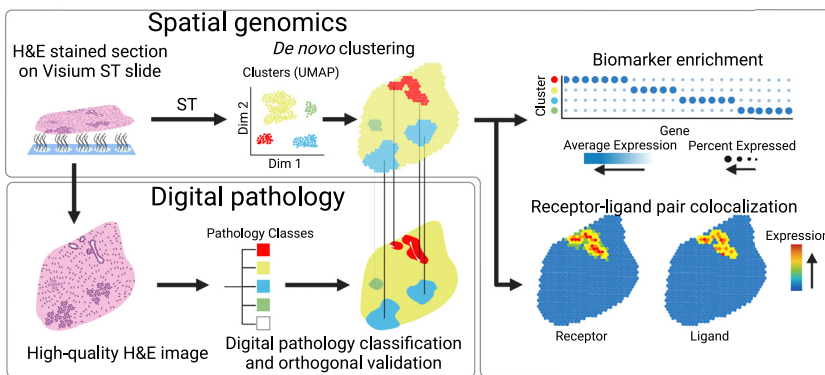
The application of ST in oncology requires that several special considerations and challenges be addressed. First, tumors are highly heterogeneous and can form disordered malignant structures admixed within normal tissue, unlike the well-structured tissues (e.g., spinal cord) used in early ST studies.²⁰ This characteristic necessitated an assessment of ST resolution and performance specifically in tumor tissue. Second, the



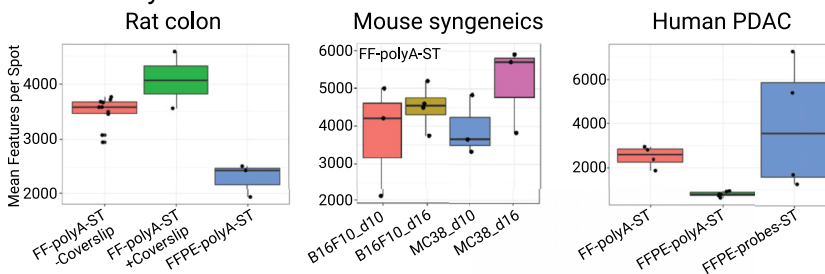
A Experimental summary

	System and modality	Goal	Conclusion
Figure 2	Rat colon 	Determine resolution, fidelity, and reproducibility of ST using a normal, well structured tissue with our spatial validation framework	ST can reliably and with high resolution capture spatial information consistent with pathology annotation and known cell types
Figures 3-4	Syngeneic tumors 	Assess the ability of ST to capture tumor and microenvironment heterogeneity in a reductionist model	ST reflects inter and intra-tumoral heterogeneity, including immune infiltration and depth-specific biology, in two mouse syngeneic oncology models
Figure 5	Single donor 	Use a single donor to compare frozen and FFPE ST modalities to support viability of ST for FFPE clinical cohorts	The FFPE probes-based ST protocol was consistent with polyA-based frozen and FFPE protocols, with few notable exceptions due to non-specific probes
Figures 6-7	Clinical cohort 	Determine the utility of ST for putative target discovery in a clinical cohort	Analysis of a small clinical cohort with our spatial validation framework showed consistency between ST and digital pathology and allowed for the identification of putative tumor biomarkers

B Spatial validation framework



C ST library metrics



specimens most broadly used for clinical pathology analysis and most readily available for molecular profiling are formalin-fixed, paraffin-embedded (FFPE) tissues.²¹ FFPE tissues have poorer transcriptome quality compared with the fresh frozen (FF) samples that have been sequenced in most spatial genomics studies to date.^{18,19,22–26} A careful comparison between frozen and FFPE protocol performance is required to provide guidance for appropriate tissue sample selection. Third, tran-

Figure 1. Experimental summary and spatial validation framework

(A) Summary of key questions addressed in this study, including cohorts, model systems, modalities, goals, and conclusions.

(B) Schematic of our spatial validation framework using high-quality imaging and digital pathology classifications to provide orthogonal validation of spatial genomics data used for biomarker discovery and target identification.

(C) Mean features identified per spot under tissue for each tissue type and protocol. Created with BioRender.com.

scriptomic maps produced by an ST experiment can be overlaid with pathology analysis, representing an opportunity to augment and validate transcriptomic measurements with other standard and advanced histologic imaging data. However, the fidelity of these multi-modal measurements (imaging and expression) needs validation and subsequent integration. Lastly, the existing spatial genomics technology profiles cell mixtures rather than single cells, necessitating an adjustment to existing genomics analytical frameworks to accommodate these low-bulk spatial outputs.

To address these challenges, we undertook a systematic assessment of ST spanning a diverse set of tissue types, sample formats, RNA capture chemistries, and computational frameworks (Figure 1A; STAR Methods). To establish our assays and analysis pipeline, we included a well-structured non-malignant tissue, two mouse syngeneic tumor models with disparate tumor microenvironments (TMEs), and clinical tumor specimens with a range of typical heterogeneous tissue compositions. We evaluated the performance of multiple ST protocols including polyA-based ST using FF tissue (herein referred to as FF-polyA-ST), as well as polyA- and probe-based transcriptome capture strategies using FFPE tissues (herein referred to as FFPE-polyA-ST and FFPE-probes-ST, respectively). We

developed a framework for gene expression and digital pathology integration from, herein referred to as, the spatial validation framework (Figure 1B). It enables the validation of expression data distribution and interpretation using histology, which is the gold standard for characterizing tissue architecture. We also tested if current single-cell genomics approaches for target identification can be applied to spatial genomics.

To facilitate the exploration of spatial genomics data, we developed a visualization application called the BMS Spatial Portal and released our data (http://periscopeapps.org:3838/spatial_portal/). This application enables the visualization of gene-expression signatures^{27–62} (Table S1) and biomarkers described in this work across all three cohorts.

Our work provides a clear framework for the application of spatial genomics for tissue characterization and putative target selection, including the utility of both frozen and FFPE samples, the efficacy of different capture chemistries, and the need for transcriptome augmentation with pathology. The resulting pilot dataset demonstrates the value of spatial genomics by revealing a high level of heterogeneity within tumor tissues, identifying shared and disparate features across tumors, characterizing the performance of commonly used cell-type biomarkers, and identifying a set of putative interactors between key spatial domains.

RESULTS

Suitability of ST to recover known tissue architectures and cell types in frozen, normal, well-structured tissue

Normal, well-structured FF tissues such as brain⁶³ or colon³³ provide simple histologic benchmarks to assess and optimize spatial genomics methods. We selected rat colon to assess the accuracy and fidelity of ST because it offers regular histology, providing a path to orthogonal validation of gene-expression measurements. We established a framework (Figure 1B) that leverages a high-resolution digital pathology annotation of tissue sections to validate the transcriptomics readout (Figure S1A; STAR Methods). This framework necessitated optimization of both the transcriptomics and imaging protocols and careful testing of whether imaging requirements, such as coverslip placement, introduced artifacts to RNA capture.

We selected normal adult rat colon, which contains both histologically well-organized compartments as well as rare cell types with well-characterized marker genes (FF-polyA-ST).³³ We compared spatial expression data generated from sections processed with or without coverslips (4 sequential tissue sections total, 2 per condition). Broadly, both datasets identified hallmark compartments (e.g., epithelium, muscle) and rare cells (e.g., enteric neurons) expressing well-established marker gene signatures (Figures 2A–2C and S1B–S1D; Table S1).³³ We compared pseudo-bulk gene expression for both conditions and observed no significant differences in pseudo-bulk gene expression between tissues processed with or without coverslips (Figure 2D). We also integrated all 4 samples, which revealed concordant *de novo* clusters regardless of whether a coverslip was used or not (Figures 2E–2H, S1E, and S1F).

We leveraged morphologic histology to assess how well the FF-polyA-ST protocol captured tissue architecture. Using supervised digital pathology approaches, we identified 8 distinct image textures that match expected major and minor colon tissue compartments (e.g., major: crypts; minor: mucosa muscularis) (Figures 2I and S1G; STAR Methods); then, we compared the spatial distribution of histology compartments with spatially agnostic *de novo* gene-expression clusters (Figures 2J and S1H). Concordantly, these clusters expressed previously re-

ported biomarkers (Figures 2H and S1F; Table S2) reflective of expected cell types within these histology compartments (Figures 2I, 2J, S1G, and S1H): muscularis propria (cluster 0), submucosa (cluster 3), crypts (cluster 1 and 4), and colonocyte border (cluster 2) with corresponding cell-type biomarkers (e.g., myocytes, fibroblasts, and enterocytes). Although the lamina propria (cluster 7), mucosa muscularis (cluster 3 and 4), and myenteric plexus (neuron biomarkers, cluster 6) were too small to cover whole spots (Figure S1G), their biomarkers were also identified *de novo* in their respective clusters.

To demonstrate the reproducibility and the technical variability of the technology, we profiled 11 additional tissue sections of rat colon ($n = 15$ sections total; 4 ST slides; Figures S1I and S1J; Table S2). We observed minimal variability between tissue sections, with the biggest source of artifacts arising from anatomical tissue variability, handling, and placement on the slide (Figures S1K–S1N). Together, these data demonstrate that FF-polyA-ST can reliably and reproducibly capture spatial expression reflective of both tissue histology and expected cell types within compartments.

Suitability of ST to recover known tumor heterogeneity in syngeneic mouse models

We next sought to assess whether spatial genomics captures tumor heterogeneity and microenvironment features using well-characterized mouse models. Spatial architecture of mouse tumor models is simple compared with human tumor tissue and presents an opportunity to benchmark ST performance for tumor biology. We leveraged two syngeneic mouse models, murine melanoma B16F10 (B16F10) and murine colon adenocarcinoma 38 (MC38), which have disparate TMEs. B16F10 is a pigmented melanoma model that forms immunologically cold tumors, while MC38 model is highly fibrotic and immune infiltrated.⁴⁰

We profiled syngeneic tumors from subcutaneously injected murine B16F10 or MC38 cells using FF-polyA-ST and applied our spatial validation framework to these data to characterize both the tumor and the TME (Figures 3A–3F and S2A–S2I). To explore technical variability, we profiled one subcutaneously grown tumor from one mouse with 3 sequential tumor sections for each model ($n = 6$; STAR Methods), and to capture biological variability, we profiled three different tumors from three animals with 1–2 sequential tumor sections for each animal ($n = 7$; STAR Methods). Both technical and biological replicates had high pseudo-bulk correlation ($R \sim 0.99$ and 0.98 , respectively, for each cohort; Figures S2D and S2E), and key tumor, fibrotic, and immune biomarkers had high concordance within each respective model (Figures S2C and S2H–S2I; Table S3). Unlike the above characterized rat colon, syngeneic tumors are relatively histologically homogeneous; however, we used digital pathology to identify tumor core, melanin deposits, and necrotic regions across all tumors (discussed below; Figures 3C, 3D, S2A, S2B, and S2J–S2N).

The integrated ST data for B16F10 and MC38 tumor cohorts broadly recapitulated known biology for both tumor models. B16F10 tumors expressed very high levels of genes involved in melanin production and packaging (*Tyrp1*, *Dct*, *Pmel*, and *Mlana*), and melanin deposits were visible in tumor section images (Figures 3E and S2N; Table S3).⁵¹ MC38 tumors expressed

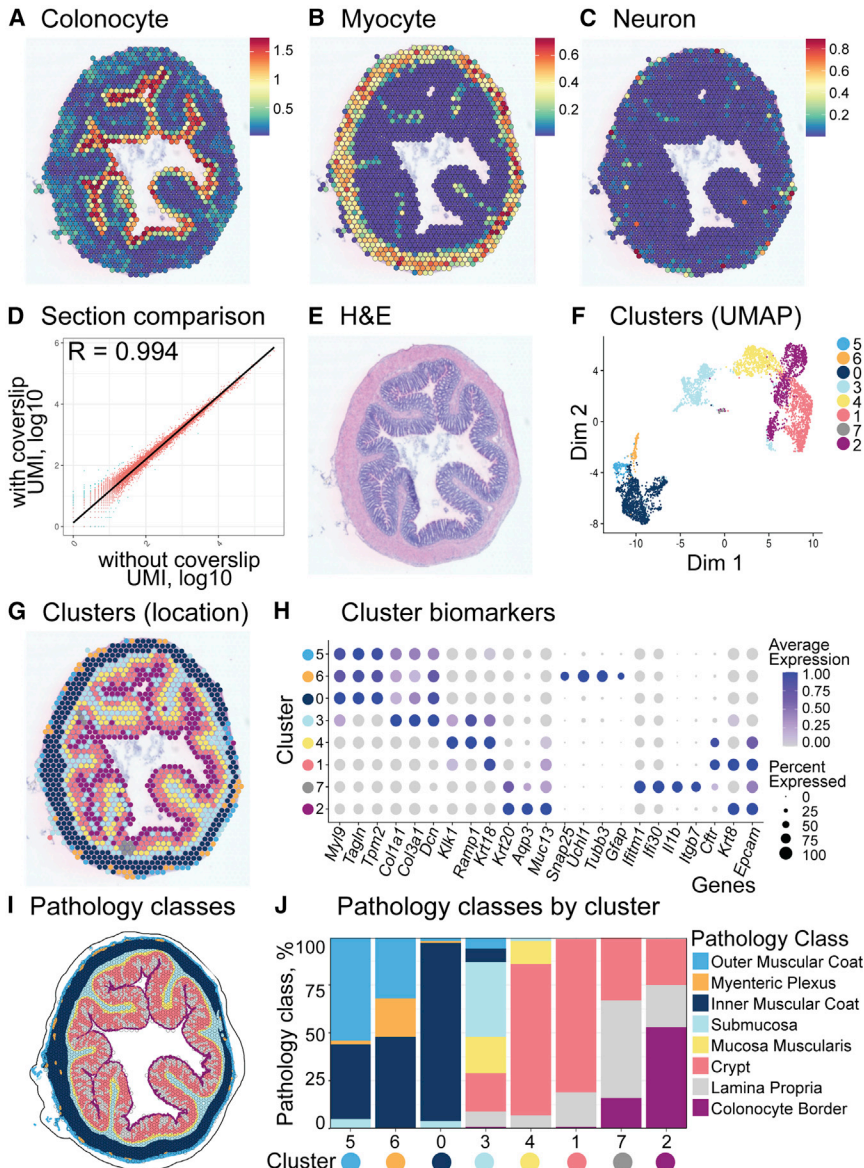


Figure 2. ST recovers known tissue architectures and cell types in frozen, normal, well-structured tissue

(A–C) Gene expression signatures on a representative fresh-frozen rat colon section for colonocytes (A), myocytes (B), and neurons (C) as detected by ST. Sections imaged and processed with a coverslip. Scale bars represent average SCT-normalized expression levels of gene signatures (STAR Methods).

(D) Pseudo-bulk gene expression comparison from ST data between fresh-frozen rat colon sections processed with a coverslip or without a coverslip ($n = 2/\text{condition}$).

(E) Representative bright-field image of an H&E-stained frozen rat colon section used for ST.

(F–H) *De-novo*-derived ST clusters and biomarkers for rat colon.

(F) Uniform manifold approximation and projection (UMAP) embedding of spot expression profiles (dots) colored by *de novo* cluster.

(G) Spatial visualization of tissue sections colored by cluster.

(H) Corresponding cluster biomarkers (dot size: fraction of spots expressing each biomarker; dot color: mean expression level in expressing spots).

(I and J) Tissue compartments as identified by digital pathology.

(I) Textures as identified by digital pathology overlaid on the colon section. Colors represent distinct textures and are matched to pathology annotations (legend, right).

(J) Comparison of transcriptional *de novo* cluster spot assignments and digital pathology textures. Clusters are numbered and depicted along the x axis. Digital pathology composition of each cluster is represented by the corresponding bar graph.

MC38 markers (*Shisa12B* and *Rhox5*), as well as markers of macrophages (*Cd74* and *Csf1r*), fibroblasts (*Col3a1*, *Dcn*, and *Col6a1*), and interferon response (*Cxcl9*, *Cxcl10*, and *Cd274*), which were largely excluded from B16F10 tumors (Figure 3F; Table S3).^{40,42}

Both tumor cohorts displayed remarkable levels of spatial gene-expression heterogeneity and shared some prominent features. The dominant cluster (cluster 0; Figures S2F and S2G) in each syngeneic model was enriched for tumor cells and expressed the highest levels of canonical biomarkers for each cell line (Figures 3E, 3F, S2H, and S2I). Both models contained a robust hypoxic compartment (cluster 2 in both cohorts; Figures 3A, 3B, S2F, and S2G), which shared key biomarkers including *Aldoa* and *Ier3* (Figures 3E and 3F).^{64,65} Finally, both models contained clusters corresponding to pathology-derived

necrotic regions (clusters 1 and 4 for B16F10; cluster 3 for MC38; Figures 3A–3D, S2A, S2B, S2F, S2G, S2J, and S2O). Necrotic clusters exhibited fewer detected genes and expressed biomarkers attributable to cell cycle and stress (Figures S2H–S2K and S2O–S2P; Table S3). Spatially, hypoxic clusters were more centrally distributed compared with the necrotic clusters in both models (Figures S2L–M and S2Q–S2R). Although B16F10 tumors had a significantly lower proportion of cancer-associated fibroblasts (CAFs) and CAF biomarker expression compared with MC38⁴⁰ (Table S3), we detected a peripherally trending region (cluster 3) in the B16F10 cohort enriched for fibrotic and extracellular matrix biomarkers (e.g., collagens; Figures 3A, 3E, S2F, and S2H; Table S3). Given that, the detection of fibrotic pockets has implications for testing putative TME targets.

ST recovers TME features within frozen, syngeneic tumors

The utility of ST to dissect cancer interactions depends on its ability to resolve the TME. Relative cell-type localization is a

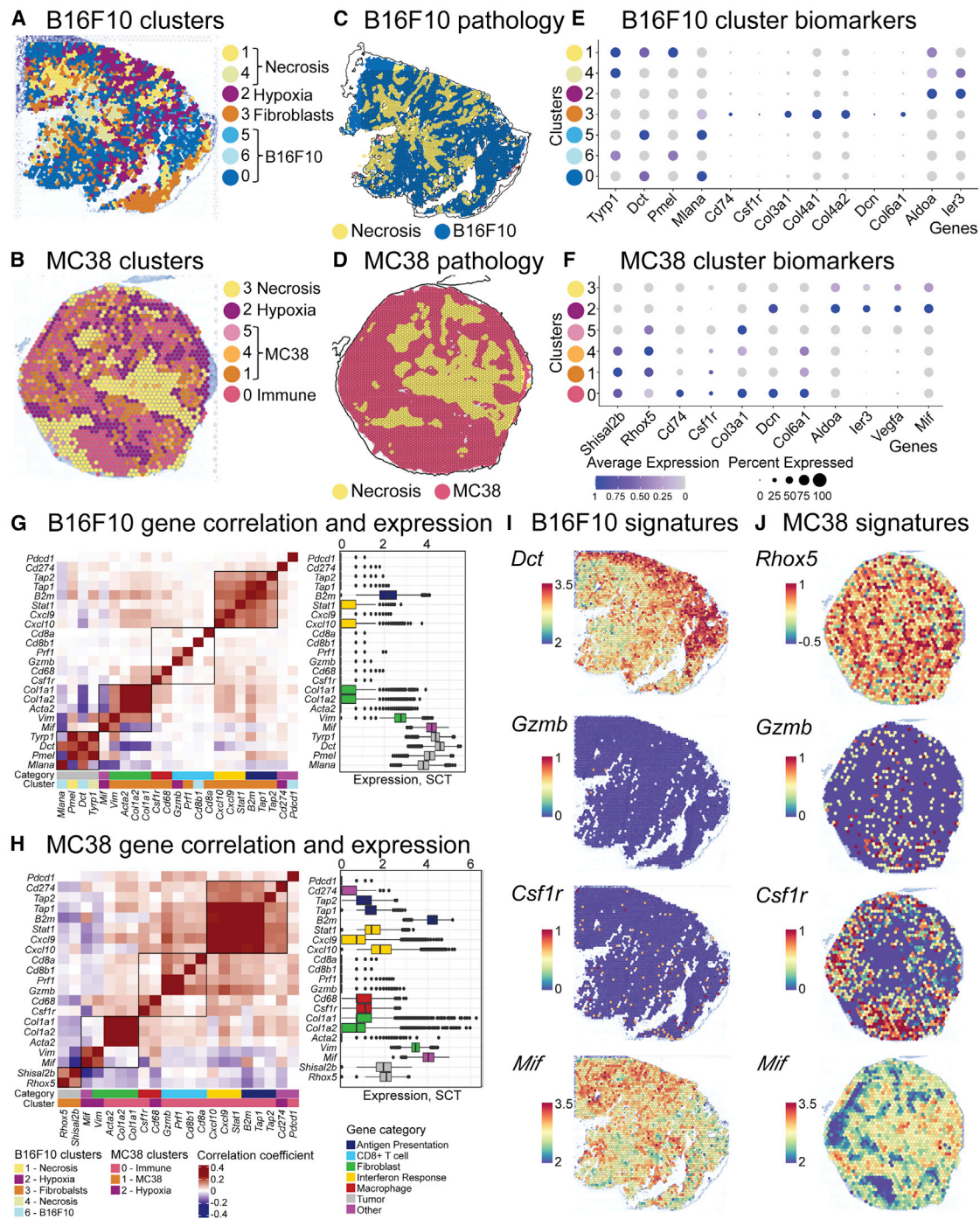


Figure 3. ST recovers known tumor heterogeneity in syngeneic mouse models

(A–F) B16F10 (n = 7; see also Figure S2A) or MC38 (n = 6; see also Figure S2B) syngeneic tumor cohorts were profiled using ST. One representative section is visualized for each of the models; full cohort plots are available in Figure S2.

(A and B) *De-novo*-derived clusters are visualized spatially for representative B16F10 (A) and MC38 (B) sections.

(C and D) Digital pathology identification of tumor (blue for B16F10; red for MC38) and necrosis (yellow) compartments in representative tissue B16F10 (C) and MC38 (D) sections.

(E and F) *De-novo*-derived cluster biomarkers for B16F10 (E) and MC38 (F) tumor cohorts (dot size: fraction of spots expressing each biomarker; dot color: mean expression level in expressing spots).

(G and H) Pairwise correlation of canonical cell-type marker gene expression across all spots in B16F10 (G) and MC38 (H) tumor cohorts.

(I and J) Gene expression of select canonical cell-type markers for B16F10 (I) and MC38 (J) tumors. Scale bars represent SCT-normalized gene expression levels (STAR Methods).

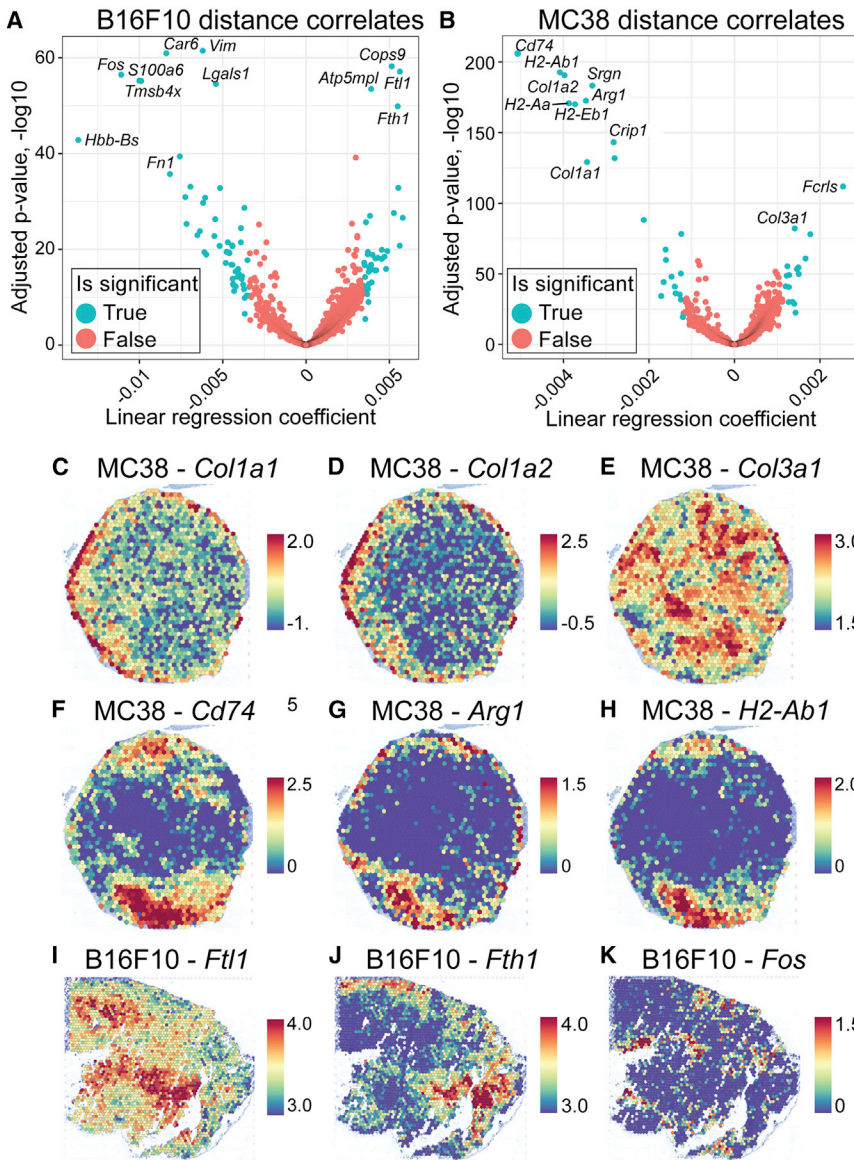


Figure 4. ST recovers tumor microenvironment depth correlates in syngeneic tumors
(A and B) Gene expression profiles associated with the edge-to-center depth of B16F10 (A) and MC38 (B) tumors (x axis: linear model coefficient estimate; y axis: $-\log_{10}$ adjusted p value). (C–K) Spatial visualization of select genes with transcriptional profiles strongly associated with tumor depth, i.e., upregulated expression in either the periphery or center of either B16F10 or MC38 tumors (mouse model and gene indicated in panels). Scale bars represent SCT-normalized gene expression levels (STAR Methods).

were observed in the same *de novo* cluster in both models (clusters 3 and 1 in B16F10 and MC38 cohorts, respectively; Figures 3A and 3B), they had discrete areas of localization, and macrophages were anti-correlated with *Mif* (Figures 3G–3J), which limits macrophage movement within tissue.^{74–76} This demonstrates that correlative approaches to spatial genomics syngeneic data can elucidate relative localizations of previously characterized immune phenotypes.^{40,71,77}

We next sought to assess whether ST could resolve common and model specific depth correlates in syngeneic tumors. We leveraged spatial context by looking for transcriptional associations with the distance between each capture spot within the tumor and the tumor edge. We examined correlates in both models and found that strong depth correlates were tumor-type specific (Figures 4A, 4B, and S3; Table S4). In the MC38 cohort, the strongest distance correlates were either collagens or macrophage biomarkers and major histocompatibility complex (MHC) class II-

associated genes (Figure 4B). *Col1a1* and *Col1a2* were enriched along the periphery and strongly associated with *de novo* cluster 5, while *Col3a1* was enriched in the interior of MC38 tumors and not associated with a specific cluster (Figures 4C–4E and S3A–S3C). Type I collagens, including *Col1a1* and *Col1a2*, facilitate tumor growth inhibition by activating fibroblasts,⁷⁸ while *Col3a1* is associated with poor prognosis in colorectal cancer.⁷⁹ Macrophages (*Cd74*, *Arg1*) and MHC class II genes (*H2-ab1*, *H2-aa*, *H2-eb1*) were generally co-localized, though *Cd74* was expressed most broadly, and *Arg1* was peripherally bound (Figures 4F–4H and S3D–S3F). This observation is consistent with previous findings demonstrating that *Arg1* is expressed in a subset of peripheral, immune-suppressive tumor-associated macrophages (TAMs) in MC38 tumors.⁸⁰ In the B16F10 cohort, both heavy and light ferritin chain genes (*Fth1* and *Ftl1*) were expressed at higher levels in the tumor center. Though *Ftl1* and

key feature of the TME,⁶⁶ with tumor depth being of particular importance in mouse models. We assessed if ST can uncover tumor depth correlates, focusing on established features such as hypoxia, necrosis, and the extracellular matrix.^{67–70}

To examine if ST could resolve the co-localization of different cell types in the microenvironment, we examined the spot-by-spot correlation of canonical cell-type markers in the syngeneic cohorts. This revealed that for both tumor models, the tumor compartment was anti-correlated with adaptive and innate immune markers (Figures 3G and 3H), reflecting immune cell localization to focal regions of the tumor rather than an even distribution throughout tumor tissue.^{71–73} This observation is particularly apparent in the MC38 cohort due to the relatively higher expression of immune biomarkers compared with the B16 model (e.g., *Gzmb* and *Csf1r*; Figures 3I and 3J). Interestingly, though the highest levels of T cells and macrophages

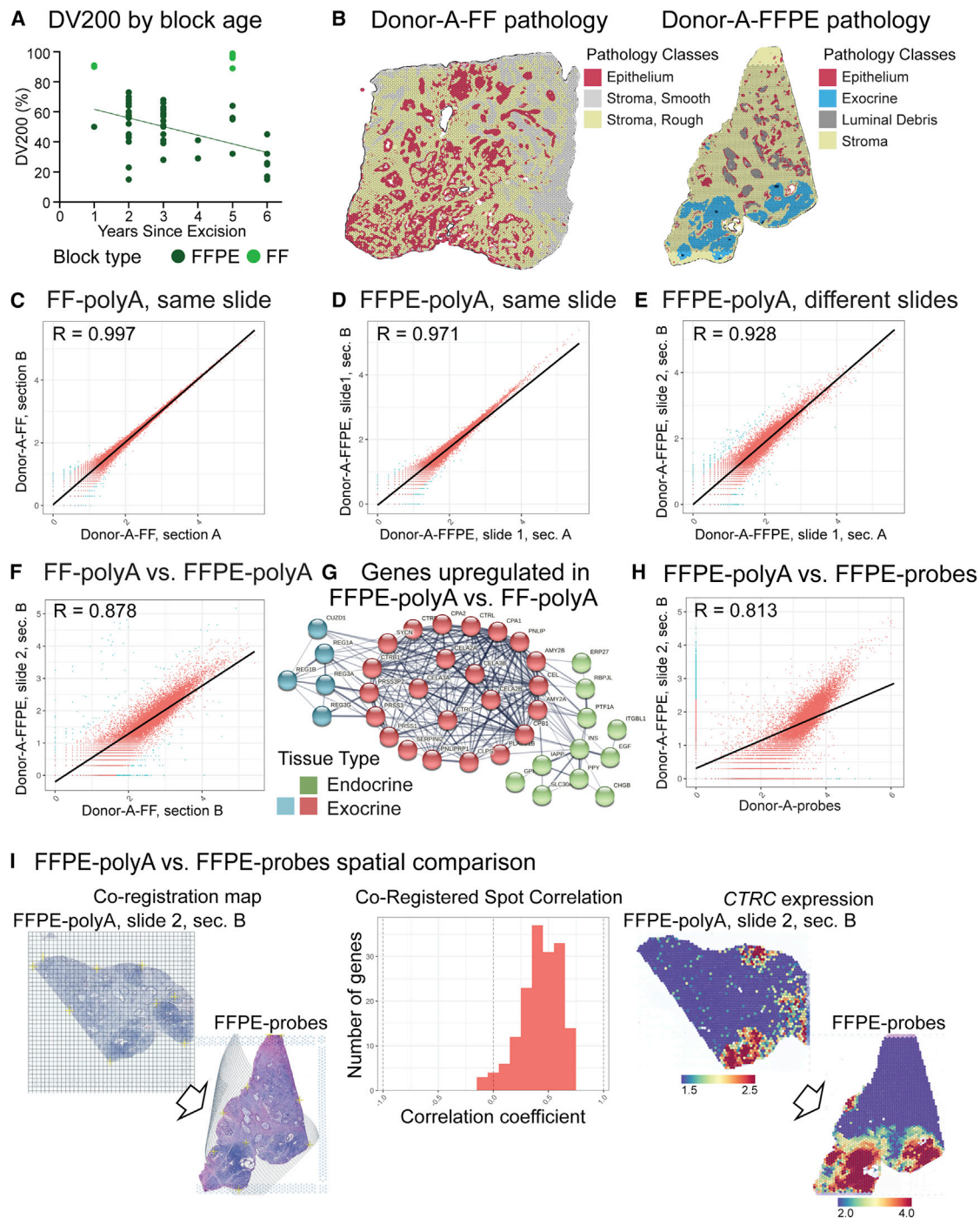


Figure 5. Comparison of polyA- and probe-based chemistries for matched fresh frozen and FFPE samples from a single PDAC donor

(A) Quality measurement (DV200) of RNA from human tumor FFPE blocks relative to time post-excision and preservation (dark green). DV200 for fresh frozen (FF) tissue relative to time post-excision and preservation (light green).

(B) Composition of donor A-FF (left) and -FFPE (right) tumor blocks. H&E-stained pathology sections were characterized using digital pathology, with respective classifications displayed.

(C–F) Concordance of transcriptome capture across ST profiled sections as assessed by pseudo-bulk correlation for FF-polyA-ST versus FF-polyA-ST on the same slide (C), FFPE-polyA-ST versus FFPE-polyA-ST on the same slide (D), FFPE-polyA-ST versus FFPE-polyA-ST on different slides (E), and FF-polyA-ST versus FFPE-polyA-ST on different slides (F).

(G) Gene set enrichment analysis of ST expression from donor A-FFPE and -FF tumor blocks. Network diagram displays genes upregulated in FFPE block, which is enriched for tumor-adjacent normal exocrine and endocrine tissue.

(legend continued on next page)

Fth1 are often co-expressed (CCLE Database) and high serum ferritin is associated with cancer,⁸¹ the two genes had distinct spatial localizations (Figures 4I, 4J, S3G, and S3H). In contrast, *Fos* was expressed in the B16F10 tumor periphery in small, localized regions (Figures 4K and S3I). Such depth-dependent correlations may be usefully leveraged in future studies to further characterize tumor architecture and heterogeneity.

Above, we describe three approaches to characterize the tumor and microenvironment heterogeneity in reductionist systems: spatially agnostic *de novo* clustering typical for single-cell studies, correlative co-expression analysis that relies on the low-bulk nature of ST data and treats each capture spot as a neighborhood of cells, and transcriptional feature selection using pathology-derived gradients. Each of these methods uncovers different types of biology and can enable dissection of differential tumor responses to targeted perturbations and treatments and better localization of pharmacodynamic responses.

Comparison of polyA- and probe-based chemistries for matched FF and FFPE samples from a single PDAC donor

While most spatial genomics studies have used FF tissue, clinical specimens are more broadly available as FFPE blocks, the format typically used for clinical pathology analysis. However, while FFPE samples can remain suitable for histological assessment for many years, the RNA within these tissues becomes fragmented and chemically modified, making genomics studies more difficult with a limited post-excision window for transcriptomic utility (~3–5 years; Figure 5A). This transcriptome deterioration raises the need to understand technology utility for banked FFPE samples. To address the suitability of spatial genomics for patient tumor characterization, we systematically appraised the performance of ST in clinical FFPE cancer samples, deeply for a single donor and then for a larger cohort.

Pancreatic ductal adenocarcinoma (PDAC) is highly fibrotic, with low cellularity, and contains autolytic enzymes.⁸² We characterized a PDAC tumor taken from a single donor (donor A) that was divided upon collection into two blocks: one portion snap frozen (donor A-FF) and the other FFPE (donor A-FFPE). Notably, the two donor A blocks significantly varied in tissue feature composition. The donor A-FF block consisted primarily of infiltrating tumor tissue, and the donor A-FFPE block contained significant tumor-adjacent normal pancreas (Figures 5B, S4F, S4G, S5F, and S4G).

We applied the FF-polyA-ST protocol and the Lundberg FFPE-polyA-ST protocol to the corresponding donor A blocks. Each block was profiled with at least four sequential tissue sections and analyzed using our spatial validation framework (Figure 1B). Although the FFPE-polyA-ST protocol resulted in a reduced unique molecular identifiers (UMIs) and gene recovery compared with the FF-polyA-ST protocol (Figure 1C; STAR Methods), sequential sections from both donor A-FF and donor A-FFPE were remarkably internally consistent ($R = 0.997$ and

0.971 , respectively; Figures 5C and 5D). Given the lower UMI recovery for FFPE-polyA-ST, we compared recovery across multiple slides and found a high concordance ($R = 0.928$; Figure 5E), supporting that transcriptome recovery is an inherent block property. We then compared transcriptome capture between FF-polyA-ST and FFPE-polyA-ST protocols and found high concordance ($R = 0.878$; Figure 5F), with differences arising from the high content of normal pancreatic tissue in the FFPE block (Figure 5G; Table S5).

An alternative to the FFPE-polyA-ST protocol is a surrogate measure of gene expression that uses gene-specific probe pairs to detect transcripts (Visium Spatial Gene Expression for FFPE, 10x Genomics). To evaluate this technology, we applied the Visium probe-based protocol (FFPE-probes-ST) to one section of the previously characterized donor A-FFPE block. The FFPE-probes-ST protocol recovered significantly more features per spot (7,265 versus 899 genes per spot on average; Figure 1C; STAR Methods), and the transcriptional pseudo-bulk gene expression matched FFPE-polyA-ST data ($R = 0.813$; Figure 5H), with notable exceptions (183 outlier genes as defined in STAR Methods; Table S5) that could be attributed to key genes missing from the probe library (e.g., *PRSS2*, an acinar biomarker) and probes that lacked specificity for their target genes (e.g., *REG1B*). To directly compare FFPE-polyA-ST and FFPE-probes-ST, we spatially co-registered two sections (Figure 5I) and observed that most well-expressed genes had well-correlated spatial distributions across tissue compartments (e.g., *CTRC*, an acinar marker gene; Figure 5I). Finally, we successfully integrated FFPE-probes-ST data with the FFPE-polyA-ST data and identified consistent compartments and biomarkers (Figures S5A–S5C).

Digital pathology augmentation validates transcriptomics capture of macroscopic heterogeneity in PDAC tumors

Patient tumors are histologically complex structures consisting of diverse cell types and states, which result in extensive transcriptional heterogeneity and a multitude of TME features.^{83–86} In such tissues, matching transcriptionally distinct regions to corresponding pathology structures is key to data interpretation. We demonstrate the accuracy of ST transcriptome capture and resulting tumor tissue characterization by matching transcriptomic data to pathology from the same tissue sample. In one example, we show how this approach identifies the misattribution of established tumor gene signatures to normal tissue (described below).

We built a cohort of four different PDAC regions from three patients across all three ST technologies (FF-polyA-ST, FFPE-polyA-ST, and FFPE-probes-ST) with a total of 12 PDAC sections (Figures 6A–6D, S4A, S5A, S6A, and S6D). Independently, each section was characterized using digital pathology segmentation (Figures 6I, S4F, and S5F), revealing that the cohort contained significant macroscopic tissue heterogeneity (Figures S4G, S5G, S6A, and S6D), with varying levels of tumor

(H) Concordance of transcriptome capture across ST profiled sections as assessed by pseudo-bulk correlation for FFPE-polyA-ST versus FFPE-probes-ST.

(I) Correlation of gene expression from spatially co-registered FFPE-polyA-ST and FFPE-probes-ST sections. H&E images of sections and co-registration (left). Correlation of expression of sufficiently expressed genes across all co-registered spots (center) between two protocols. Representative spatial gene expression of concordant biomarker, *CTRC* (right).

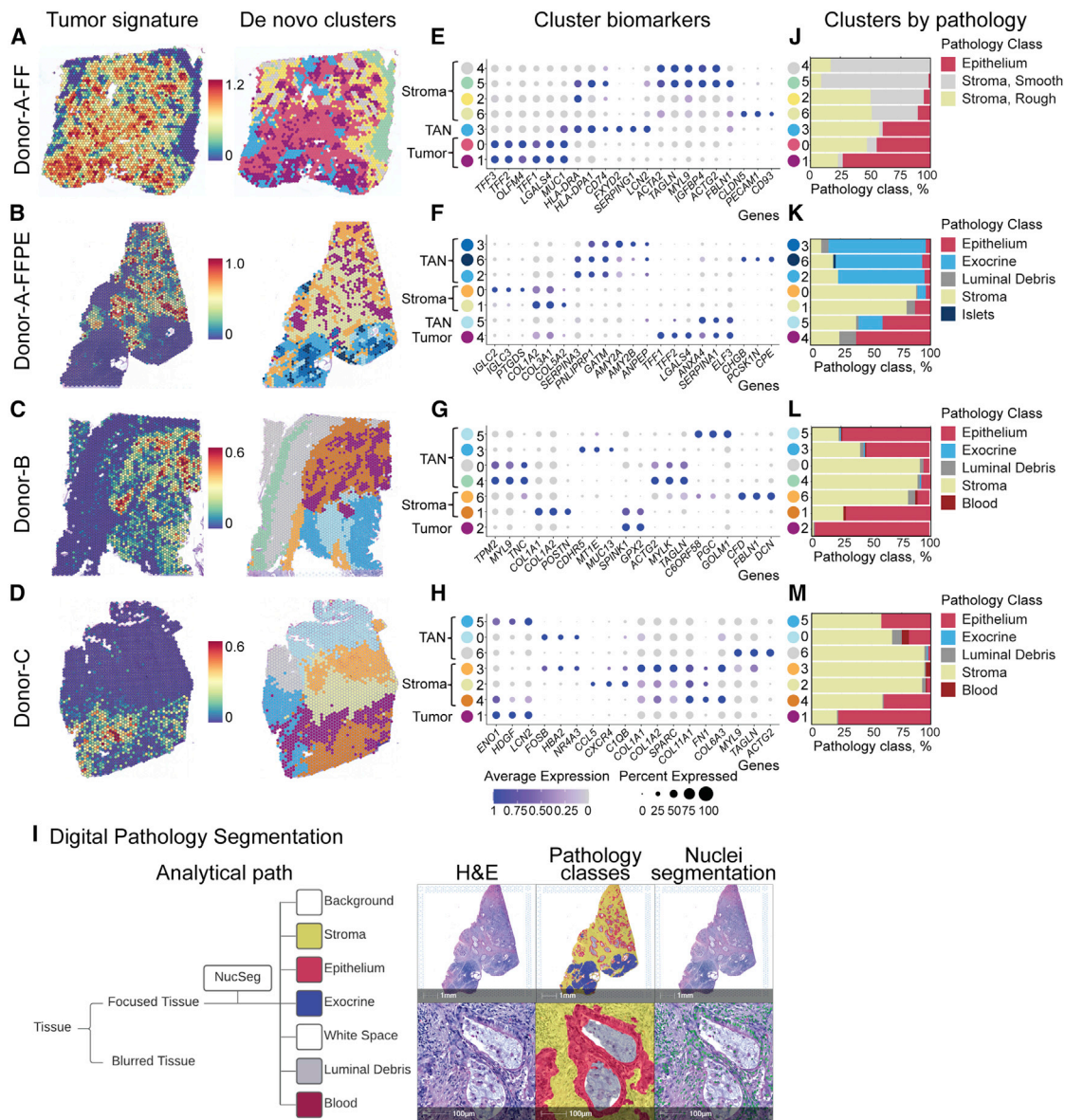


Figure 6. Digital pathology augmentation validates transcriptomics capture of macroscopic heterogeneity in PDAC tumors

(A–D) Spatial visualization of PDAC tumor signature (left) and *de novo* expression clusters (right) for representative sections from donor A-FF FF-polyA-ST (A), donor A-FFPE FFPE-probes-ST (B), donor B FFPE-probes-ST (C), and donor C FFPE-probes-ST (D) sections. Tumor signature is the classical PDAC signature from Collison et al.³² and highlights tumor regions in red. Scale bars represent average SCT-normalized expression levels of gene signatures (STAR Methods). (E–H) *De-novo*-derived biomarkers for each PDAC tissue and cluster in (A)–(D) (E: donor A-FF FF-polyA-ST; F: donor A-FFPE FFPE-probes-ST; G: donor B FFPE-probes-ST; H: donor C FFPE-probes-ST) (dot size: fraction of spots expressing each biomarker; dot color: mean expression level in expressing spots). (I) Digital pathology framework (left) and representative segmentation by texture and nuclei (right) for donor A-FFPE FFPE-probes-ST. (J–M) Overlay of transcriptional clusters and digital pathology textures. Clusters are numbered and depicted along the y axis. Digital pathology composition of each cluster is represented by the corresponding bar graph (J: donor A-FF FF-polyA-ST; K: donor A-FFPE FFPE-probes-ST; L: donor-B FFPE-probes-ST; M: donor C FFPE-probes-ST).

infiltration, stromal content, and tumor-adjacent normal tissue (TAN). Applying our spatial validation framework (Figure 1B) to the cohort, we first characterized the spatial heterogeneity of these samples using *de novo* clustering and then demonstrated the concordance of emerging tissue compartments with the pathology annotation of the tissue. Below, we summarize observa-

tions by donor block, and in the next section, we discuss the integrated cohort for the purposes of deriving putative therapeutic targets.

The donor A-FF cohort ($n = 4$; Figures 5B, 6A, and S4A) is comprised primarily of invasive carcinoma (clusters 0 and 1) with surrounding immune (cluster 2), stromal (cluster 4 and 5),

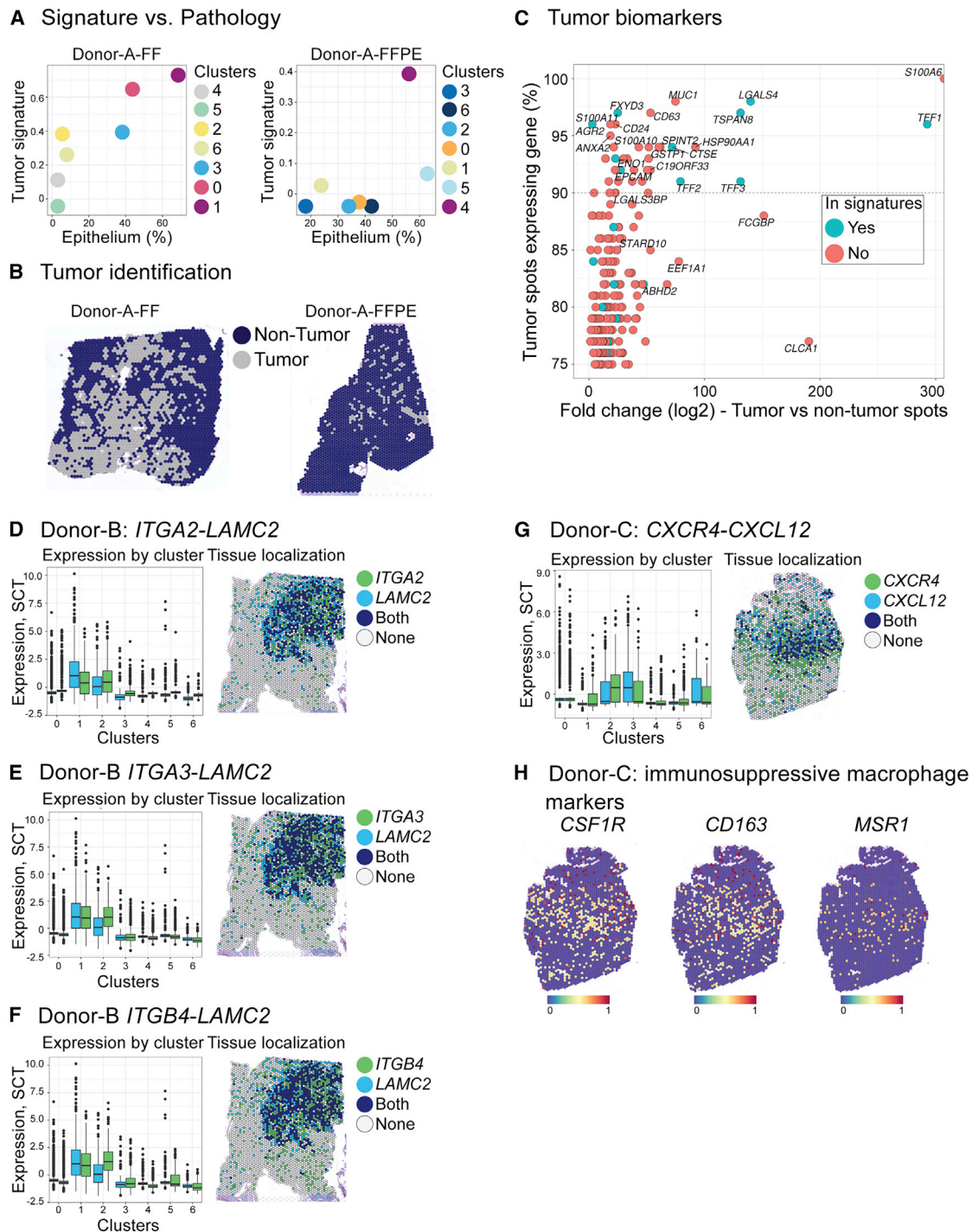


Figure 7. Derivation of tumor compartment biomarkers and putative targets from PDAC donor samples

(A) Augmentation of transcriptome-based tumor compartment identification with digital pathology. Data from two cohorts are shown: donor A-FF FF-polyA-ST (left) and FFPE-probes-ST (right). Each *de novo* expression cluster is characterized by its average score of the classical PDAC signature from Collison et al.³² (y axis) and epithelium density (x axis).

(B) Categorizing each spot in PDAC tumor samples into tumor (gray) and non-tumor (blue) using both pathology and expression data: representative characterization for donor A-FF FF-polyA-ST (left) and FFPE-probes-ST (right).

(legend continued on next page)

and vascular components (cluster 6) (Figures 6A, 6E, and S4A–S4C; Table S6). The two tumor clusters (clusters 0 and 1) are identified by a single pathology compartment but are found to be transcriptionally distinct in all four replicates (Figures S4A–S4C). The donor A-FFPE cohort is dominated by stroma and immune components (clusters 0 and 1) and TAN (clusters 2 and 3) (Figures 6B, 6F, and S5A–S5C; Table S6). Strikingly, given the large TAN component, islets of Langerhans, which are small structures, are transcriptionally resolved to contain *PPY*, *INS*, and other hallmark genes (cluster 6; Figures 6B, 6K, and S5A–S5C; Table S6). Lastly, malignant tissue, a minor portion of these sections, is also clearly resolved (cluster 4; Figures 6B, S5A–S5C; Table S6). The donor B section, profiled using FFPE-probes-ST, contains tumor (cluster 1 and 2) that has invaded the small intestine with major structures resolved: intestinal epithelium (cluster 3), muscularis propria (cluster 0 and 4), and Brunner’s glands (cluster 5) (Figures 6C, 6G, and S6A–S6C; Table S6). The donor C section profiled using FFPE-probes-ST contains a gradient of compartments that span vasculature, stroma, immune, TAN, and tumor compartments (Figures 6D, 6H, and S6D–S6F; Table S6). The tumor is a minority of the tissue and is layered between macrophage- and fibroblast-enriched bands.

Transcriptional characterization of the cohort agreed with the pathology annotation (Figures 6I, S4F, and S5F). Specifically, the donor A-FF cohort was epithelium and stroma dominant in the appropriate clusters (Figure 6J); the donor A-FFPE cohort contained mainly exocrine, ductal, and stromal tissue, with a minority of clusters containing epithelium (Figure 6K); the donor B section had epithelium correspond to both tumor and intestinal epithelium regions but not the muscularis mucosa (Figure 6L); and the donor C section contained minority epithelium, corresponding to the tumor band, with the remainder of the tissue classified as stroma, ducts, and vascular structures (Figure 6M). Together, these data indicate that ST can capture both major and minor tissue compartments and their corresponding gene expression across a range of tumor structures.

Derivation of tumor compartment biomarkers and putative targets from PDAC donor samples

To accurately identify the tumor compartment, we selected those capture spots that were categorized as tumor through *de novo* clustering and biomarker annotation and pathology, as well as gene expression signature score (Figures 7A, 7B, S7A, and S7B). To identify tumor regions using gene signatures, we compiled PDAC bulk RNA sequencing (RNA-seq) signatures from prior molecular subtyping efforts by Collison et al.,⁸⁷ Moffitt et al.,⁴⁴ and Bailey et al.³⁰ and calculated tumor signature scores for every capture spot (STAR Methods). Across our cohort, the Collison classical PDAC signature performed best based on the dynamic range of signature scores and concordance with

clinical pathology annotations (Figures 6A–6D and S7A), despite resolution differences between bulk RNA-seq and ST. Subsequently, we select the capture spots within the putative tumor *de novo* clusters with strong Collison classical PDAC signature and epithelium density profiles.

We next sought to understand whether we could identify tumor-specific gene expression from an integrated cohort. The intersection of gene expression signature data and pathology annotations allowed us to identify tumor regions with high confidence and compare “high tumor purity” areas with the rest of the tissue, given the extensive presence of stroma, immune, and normal compartments across the donor samples (Figures 7A, 7B, and S7C; STAR Methods). Applying differential expression analysis to the cohort, we identified a set of genes highly enriched in tumor regions compared with the surrounding heterogeneous tissue (Figure 7C; Table S7). A subset of these genes has previously been associated with PDAC progression and prognosis and range from common essential genes to known tumor-intrinsic biomarkers (Figures 7C and S7C). For example, one biomarker was *MIF*, a secreted ligand known to play a pleiotropic role in immunity and inflammation modulation to aid in tumor immune evasion,^{88,89} imalumab, an anti-MIF antibody, is currently in clinical development.⁹⁰ Another sample biomarker is *TMBIM6*, which plays a role in the progression of cancers through mTORC2 and AKT activation.⁹¹ The inherent ability of ST to allow for analysis of specific tissue compartments could facilitate the identification and prioritization of targets in both tumor and non-tumor (e.g., stromal) regions using the same samples.

Identification of autocrine and paracrine signaling in PDAC

Capturing the spatial architecture of tissue empowers the identification of relevant autocrine and paracrine signaling, which makes spatial genomics data well positioned to interrogate such interactions. In the current ST implementation, each capture spot contains 10 to 30 cells (STAR Methods), meaning that cell signaling events are captured within spots and can be identified through co-localized expression analysis of previously annotated gene pairs such as receptors and their ligands. We employed this approach by mapping receptor-ligand pairs from FANTOM5⁹² to our ST PDAC cohort (STAR Methods; Table S7). Below, we highlight two examples of interactions of mixed-stroma and tumor-enriched receptor-ligand pairs.

In donor B, the tumor epithelium (clusters 1, 4, and 6) are enriched for the integrins *ITGA2*, *ITGA3*, and *ITGB4* and their binding partner, *LAMC2* (Figures 7D–7F). *ITGA2* and *LAMC2* were recently identified as putative targets for PDAC, being both over-expressed in PDAC and inversely correlated with patient survival.⁹³ In donor C, the chemokine receptor *CXCR4* and its ligand *CXCL12* are co-expressed in stromal clusters containing a

(C) Differentially expressed genes in tumor areas (n = 3 donors, 12 sections) compared with non-tumor areas (x axis: expression level in tumor versus non-tumor; y axis: percentage of tumor-expressing spots). Genes are colored by presence or absence in established PDAC classical subtype signatures (Collison et al.,⁸⁷ Moffitt et al.,⁴⁴ and Bailey et al.³⁰).

(D–G) Representative receptor-ligand pairs mapped to PDAC tumors for donor B (D–F) and donor C (G). Receptor-ligand pairs indicated in panels.

(H) Spatial gene expression in donor C of *CSF1R* (left), *CD163* (middle), and *MSR1* (right). Scale bars represent SCT-normalized gene expression levels (STAR Methods).

mixture of fibroblasts and macrophages (clusters 2, 4, and 6) (Figure 7G). This receptor-ligand pair is associated with tumorigenesis in a variety of cancer types, including PDAC.⁹⁴ CXCL12 is secreted by CAFs and other stromal cells, acting in an autocrine fashion to drive desmoplasia and in a paracrine fashion to modulate immune cell chemotaxis.⁹⁵ Indeed, gene expression in these spots identifies the presence of immunosuppressive macrophage markers (e.g., *CD163* and *MSR1*;⁹⁶ Figure 7H). Taken together, these examples highlight the strength of leveraging receptor-ligand pair analysis to identify tumor signaling.

DISCUSSION

Deep spatial molecular profiling of cancer models and patient samples helps to identify and prioritize novel oncology drug targets and select appropriate reductionist models. In this work, we demonstrate that spatial genomics produces granular transcriptomic data in a variety of tissue types that is concordant with previous studies and can facilitate deeper disease biology insights. Furthermore, we employ multi-modal analysis of the same tissue section, bringing together pathology and genomics analytical approaches to create a high-confidence characterization that facilitates oncology target hypothesis generation.

ST data can uncover previously unseen heterogeneity within concurrently identified pathology compartments. For example, all four replicates of donor A-FF have two transcriptionally distinguishable clusters within the single tumor epithelium compartment that were identified by digital pathology. While larger cohorts would be needed to substantiate this heterogeneity, this observation points to meaningful intratumoral differences. Accounting for such heterogeneity is key to the success of oncology treatments and counter-interacting cancer resistance. Importantly, digital pathology approaches can provide a bridge between low-throughput ST data and large imaging clinical cohorts:⁹⁷ digital pathology classifiers can be trained using spatial genomics data to capture transcriptional heterogeneity and then be applied in image-only cohorts.

Other technologies combine transcriptomic and spatial information, each with different advantages and drawbacks that make them well suited for different experimental questions. For example, Lohoff and colleagues utilized a fluorescence *in situ* hybridization (FISH) method with sequential labeling (seqFISH) to localize transcripts for nearly 400 genes, resulting in single-cell spatial resolution at the cost of full-transcriptome coverage.⁹⁸ Another technology, digital spatial profiling (DSP), allows for the localization of transcripts and proteins within small pre-selected regions of interest, making it better suited for focused hypothesis testing than *de novo* discovery.⁹⁹ Selecting the best technology for a given question is an important consideration when designing these experiments.

Many efforts are underway to integrate single-cell and/or single-nuclei RNA-seq data with ST data, which lack single-cell resolution^{22,100,101} (reviewed by Li et al.¹⁰²). These integration methods seek to achieve spatially resolved, transcriptome-wide, single-cell datasets. However, only recently has the performance of these approaches been independently assessed utilizing paired single-cell and spatial data.¹⁰² Generating matched cohorts is labor and cost intensive and, in some cases, not tech-

nically feasible. For example, there are no single-cell RNA-seq protocols developed for FFPE tissues, which we used in this study. While it is possible to utilize datasets from different donors, the accuracy of this approach needs careful assessment, which is best served by dedicated future studies. For these reasons, we relied on pathology augmentation over deconvolution approaches in this work.

The joint use of both digital pathology and transcriptional data to define tissue regions is also an area of investigation.^{103–105} In this study, our focus was to use digital pathology as an orthogonal validation strategy for expression data instead. This is critical for troubleshooting emerging technologies, such as Visium, where transcript/probe diffusion and sample quality can be a major source of technical bias. In addition, leveraging digital pathology for cluster definitions could obfuscate unexpected tissue heterogeneity not captured by digital pathology classifiers.

Our study is a resource for oncology discovery efforts, providing guidance on the applicability of spatial genomics to early target biology. It elucidates the resolution of ST data, the advantages of pathology-guided augmentation, and the utility of surrogate probe-based transcriptome detection for FFPE tissue. We also release our data in a readily browsable application called the BMS Spatial Portal (http://periscopeapps.org:3838/spatial_portal/), which combines gene expression, gene signatures, and pathology annotation. Given the visual and intuitive nature of spatial genomics data, its compatibility with histologic imaging analysis, and the learnings that can be derived from its exploration, we hope this motivates future studies to do likewise.

Limitations of study

Although this study provides an assessment of the utility of spatial genomics for oncology discovery, there are key limitations that will need to be addressed by future studies. In its current embodiment, sequencing-based ST technologies recover low-bulk data comprising multiple cells per location barcode. While we demonstrate that this resolution has utility for recovering complex tumor architecture and signaling mechanisms, there are use cases where additional resolution is necessary, such as the identification of rare tumor stem cells (e.g., Batlle and Clevers¹⁰⁶). To achieve single-cell resolution with spatial context, computational solutions are necessary in the short term. Indeed, numerous deconvolution methods are already available (reviewed by Li et al.¹⁰²). In the long term, technology advances may fulfill this need by, for example, shrinking the capture spot size. However, smaller capture spots will not account for multiple cell layers within a tissue section, thus still requiring deconvolution to truly yield single-cell profiles.

Our study leverages a small clinical cohort, which is sufficient to assess technology but limited in its broader applications to better understand PDAC heterogeneity.^{107–109} It is well established that tumors display spatial heterogeneity, with the “necrotic core” serving as a hallmark example wherein core regions of solid tumors have foci of cell death relative to the tumor periphery.^{88,110} However, it is challenging to probe depth correlates in clinical tumor samples because tumors are divided for FFPE preservation, and center-to-edge architecture is not preserved. We thus pivoted to syngeneic tumors, where we could preserve the center-to-periphery axis and demonstrated that

spatial genomics can recover transcription correlates of tumor depth. Our results align well with previous TME observations (e.g., collagens^{78,79}) and motivate future studies of how tumor depth can promote the development of heterogeneity and therapy resistance in well-curated clinical samples.

Another caveat to assessing a small clinical cohort is that our PDAC samples do not span the range of possible pathology heterogeneity, and thus we cannot address the performance of data integration across a diverse set of tumor samples. In this resource, we performed fit-for-purpose integration for four independent datasets (i.e., 7 B16F10 samples, 6 MC38 samples, 4 PDAC FF samples, and 6 PDAC FFPE samples). The PDAC cohort covers 3 different experimental protocols applied to tissues from 3 different donors and 4 different regions of interest, thus creating a cohort highly heterogeneous in both biology and technical properties. The integration of all 12 samples, though technically possible, obscures meaningful characteristics of the data. Future biology-centered studies that deploy focused technologies to a large cohort will need to address how integration both facilitates the discovery of novel biology and obscures key patient-to-patient differences.

Lastly, we leverage digital pathology to validate the accuracy of ST data. The training of deep-learning models (e.g., convolutional neural nets) typically requires large-scale cohorts of labeled training data. Transfer learning was implemented to mitigate the limitation of sample size in the current study; however, the trained image segmentation models are likely to be overfit solutions owing to the limited scope of training data available. Due to the current lack of public ST datasets, the intracohort model performance was prioritized over intercohort generalizability. Despite this caveat for the trained models, the developed methods and framework are broadly applicable in ST experiments. Future studies are being designed to (1) bridge the data domain disconnect between available large-scale cohorts with sample-level/bulk resolution (i.e., clinical studies, TCGA, etc.) and limited ST cohorts with intra-sample/fine resolution and (2) increase sample sizes to permit optimizing the segmentation models for robustness against inter-patient and intercohort heterogeneity.

STAR★METHODS

Detailed methods are provided in the online version of this paper and include the following:

- **KEY RESOURCES TABLE**
- **RESOURCE AVAILABILITY**
 - Lead contact
 - Materials availability
 - Data and code availability
- **EXPERIMENTAL MODEL AND SUBJECT DETAILS**
 - Rats
 - Mice
 - B16F10 cell line
 - MC38 cell line
 - Human resected PDAC tumors
- **METHOD DETAILS**
 - Syngeneic tumor growth
 - Rat colon collection

- Syngeneic mouse tumor collection
- Fresh-frozen tissue embedding
- FFPE tissue embedding
- FFPE block DV200 evaluation
- Fresh-frozen histology
- FFPE histology
- ST section staining and library prep
- Imaging
- Sequencing
- Digital pathology deep learning model development
- Digital pathology tissue co-registration
- Tissue identification and pathology integration
- **QUANTIFICATION AND STATISTICAL ANALYSIS**
 - Promiscuous probe analysis
 - Pseudo-bulk expression analysis
 - Expression comparison of co-registered PDAC samples
 - Cohort integration and clustering
 - Marker gene identification and DEA
 - Gene signature scores and P-Values
 - Tumor depth modeling for syngeneics samples
 - Receptor-ligand pair analysis
- **ADDITIONAL RESOURCES**
 - BMS spatial portal

SUPPLEMENTAL INFORMATION

Supplemental information can be found online at <https://doi.org/10.1016/j.crmeth.2022.100340>.

ACKNOWLEDGMENTS

We thank Emma Lees and Matthew Trotter for valuable discussions and guidance.

AUTHOR CONTRIBUTIONS

Conceptualization, E.D. and A. Lyubetskaya; supervision, E.D., K. Mavrakis, K. Maclsaac, and B.C.; investigation, B.R. and A. Lewin; formal analysis, A. Lyubetskaya and A.F.; resources, I.N., C.B., T.B., E.P., R.G., S.K., A.F.-T., K. Mosure, and N.V.W.; writing – original and revisions, E.D., A. Lyubetskaya, B.R., A.F., and A.F.-T.

DECLARATION OF INTERESTS

A. Lyubetskaya, B.R., A.F., A. Lewin, I.N., E.P., R.G., S.K., A.F., K. Mosure, N.V.W., K. Mavrakis, K. Maclsaac, B.C., and E.D. are employees and shareholder of Bristol Myers Squibb.

Received: March 15, 2022

Revised: August 5, 2022

Accepted: October 21, 2022

Published: November 15, 2022

REFERENCES

1. Hanahan, D., and Weinberg, R.A. (2011). Hallmarks of cancer: the next generation. *Cell* 144, 646–674. <https://doi.org/10.1016/j.cell.2011.02.013>.
2. Ushijima, T., Clark, S.J., and Tan, P. (2021). Mapping genomic and epigenomic evolution in cancer ecosystems. *Science* 373, 1474–1479. <https://doi.org/10.1126/science.abh1645>.

3. Tabassum, D.P., and Polyak, K. (2015). Tumorigenesis: it takes a village. *Nat. Rev. Cancer* 15, 473–483. <https://doi.org/10.1038/nrc3971>.
4. Slyper, M., Porter, C.B.M., Ashenberg, O., Waldman, J., Drokhllyansky, E., Wakiro, I., Smillie, C., Smith-Rosario, G., Wu, J., Dionne, D., et al. (2020). A single-cell and single-nucleus RNA-Seq toolbox for fresh and frozen human tumors. *Nat. Med.* 26, 792–802. <https://doi.org/10.1038/s41591-020-0844-1>.
5. Naffar-Abu Amara, S., Kuiken, H.J., Selfors, L.M., Butler, T., Leung, M.L., Leung, C.T., Kuhn, E.P., Kolarova, T., Hage, C., Ganesh, K., et al. (2020). Transient commensal clonal interactions can drive tumor metastasis. *Nat. Commun.* 11, 5799. <https://doi.org/10.1038/s41467-020-19584-1>.
6. Sharma, P., Hu-Lieskovan, S., Wargo, J.A., and Ribas, A. (2017). Primary, adaptive, and acquired resistance to cancer immunotherapy. *Cell* 168, 707–723. <https://doi.org/10.1016/j.cell.2017.01.017>.
7. González-Silva, L., Quevedo, L., and Varela, I. (2021). Tumor functional heterogeneity unraveled by scRNA-seq technologies: (trends in cancer 6, 13–19, 2020). *Trends Cancer* 7, 265. <https://doi.org/10.1016/j.trecan.2021.02.001>.
8. Rozenblatt-Rosen, O., Regev, A., Oberdoerffer, P., Nawy, T., Hupalowska, A., Rood, J.E., Ashenberg, O., Cerami, E., Coffey, R.J., Demir, E., et al. (2020). The human tumor atlas network: charting tumor transitions across space and time at single-cell resolution. *Cell* 181, 236–249. <https://doi.org/10.1016/j.cell.2020.03.053>.
9. Ståhl, P.L., Salmén, F., Vickovic, S., Lundmark, A., Navarro, J.F., Magnusson, J., Giacomello, S., Asp, M., Westholm, J.O., Huss, M., et al. (2016). Visualization and analysis of gene expression in tissue sections by spatial transcriptomics. *Science* 353, 78–82. <https://doi.org/10.1126/science.aaf2403>.
10. Vickovic, S., Eraslan, G., Salmén, F., Klughammer, J., Stenbeck, L., Schapiro, D., Äijö, T., Bonneau, R., Bergensträhle, L., Navarro, J.F., et al. (2019). High-definition spatial transcriptomics for in situ tissue profiling. *Nat. Methods* 16, 987–990. <https://doi.org/10.1038/s41592-019-0548-y>.
11. Gohil, S.H., Iorgulescu, J.B., Braun, D.A., Keskin, D.B., and Livak, K.J. (2021). Applying high-dimensional single-cell technologies to the analysis of cancer immunotherapy. *Nat. Rev. Clin. Oncol.* 18, 244–256. <https://doi.org/10.1038/s41571-020-00449-x>.
12. Rodrigues, S.G., Stickels, R.R., Goeva, A., Martin, C.A., Murray, E., Vanderburg, C.R., Welch, J., Chen, L.M., Chen, F., and Macosko, E.Z. (2019). Slide-seq: a scalable technology for measuring genome-wide expression at high spatial resolution. *Science* 363, 1463–1467. <https://doi.org/10.1126/science.aaw1219>.
13. Chen, K.H., Boettiger, A.N., Moffitt, J.R., Wang, S., and Zhuang, X. (2015). RNA imaging. Spatially resolved, highly multiplexed RNA profiling in single cells. *Science* 348, aaa6090. <https://doi.org/10.1126/science.aaa6090>.
14. Eng, C.H.L., Lawson, M., Zhu, Q., Dries, R., Kouloua, N., Takei, Y., Yun, J., Cronin, C., Karp, C., Yuan, G.C., and Cai, L. (2019). Transcriptome-scale super-resolved imaging in tissues by RNA seqFISH. *Nature* 568, 235–239. <https://doi.org/10.1038/s41586-019-1049-y>.
15. Lee, J.H., Daugharthy, E.R., Scheiman, J., Kalhor, R., Yang, J.L., Ferrante, T.C., Terry, R., Jeanty, S.S.F., Li, C., Amamoto, R., et al. (2014). Highly multiplexed subcellular RNA sequencing in situ. *Science* 343, 1360–1363. <https://doi.org/10.1126/science.1250212>.
16. Lee, J.H., Daugharthy, E.R., Scheiman, J., Kalhor, R., Ferrante, T.C., Terry, R., Turczyk, B.M., Yang, J.L., Lee, H.S., Aach, J., et al. (2015). Fluorescent in situ sequencing (FISSEQ) of RNA for gene expression profiling in intact cells and tissues. *Nat. Protoc.* 10, 442–458. <https://doi.org/10.1038/nprot.2014.191>.
17. Wang, X., Allen, W.E., Wright, M.A., Sylwestrak, E.L., Samusik, N., Vesuna, S., Evans, K., Liu, C., Ramakrishnan, C., Liu, J., et al. (2018). Three-dimensional intact-tissue sequencing of single-cell transcriptional states. *Science* 361, eaat5691. <https://doi.org/10.1126/science.aat5691>.
18. Thrane, K., Eriksson, H., Maaskola, J., Hansson, J., and Lundeberg, J. (2018). Spatially resolved transcriptomics enables dissection of genetic heterogeneity in stage III cutaneous malignant melanoma. *Cancer Res.* 78, 5970–5979. <https://doi.org/10.1158/0008-5472.CAN-18-0747>.
19. Wu, S.Z., Al-Eryani, G., Roden, D.L., Junankar, S., Harvey, K., Andersson, A., Thennavan, A., Wang, C., Torpy, J.R., Bartonicek, N., et al. (2021). A single-cell and spatially resolved atlas of human breast cancers. *Nat. Genet.* 53, 1334–1347. <https://doi.org/10.1038/s41588-021-00911-1>.
20. Maniatis, S., Äijö, T., Vickovic, S., Braine, C., Kang, K., Mollbrink, A., Faggealtier, D., Andrusivová, Ž., Saarenpää, S., Saiz-Castro, G., et al. (2019). Spatiotemporal dynamics of molecular pathology in amyotrophic lateral sclerosis. *Science* 364, 89–93. <https://doi.org/10.1126/science.aav9776>.
21. Mathieson, W., and Thomas, G.A. (2020). Why formalin-fixed, paraffin-embedded biospecimens must be used in genomic medicine: an evidence-based review and conclusion. *J. Histochem. Cytochem.* 68, 543–552. <https://doi.org/10.1369/0022155420945050>.
22. Andersson, A., Larsson, L., Stenbeck, L., Salmén, F., Ehinger, A., Wu, S.Z., Al-Eryani, G., Roden, D., Swarbrick, A., Borg, Å., et al. (2021). Spatial deconvolution of HER2-positive breast cancer delineates tumor-associated cell type interactions. *Nat. Commun.* 12, 6012. <https://doi.org/10.1038/s41467-021-26271-2>.
23. Gouin, K.H., Ing, N., Plummer, J.T., Rosser, C.J., Ben Cheikh, B., Oh, C., Chen, S.S., Chan, K.S., Furuya, H., Tourtellotte, W.G., et al. (2021). An N-Cadherin 2 expressing epithelial cell subpopulation predicts response to surgery, chemotherapy and immunotherapy in bladder cancer. *Nat. Commun.* 12, 4906. <https://doi.org/10.1038/s41467-021-25103-7>.
24. Nagasawa, S., Kuze, Y., Maeda, I., Kojima, Y., Motoyoshi, A., Onishi, T., Iwatani, T., Yokoe, T., Koike, J., Chosokabe, M., et al. (2021). Genomic profiling reveals heterogeneous populations of ductal carcinoma in situ of the breast. *Commun. Biol.* 4, 438. <https://doi.org/10.1038/s42003-021-01959-9>.
25. Moncada, R., Barkley, D., Wagner, F., Chiodin, M., Devlin, J.C., Baron, M., Hajdu, C.H., Simeone, D.M., and Yanai, I. (2020). Integrating microarray-based spatial transcriptomics and single-cell RNA-seq reveals tissue architecture in pancreatic ductal adenocarcinomas. *Nat. Biotechnol.* 38, 333–342. <https://doi.org/10.1038/s41587-019-0392-8>.
26. Berglund, E., Maaskola, J., Schultz, N., Friedrich, S., Marklund, M., Bergensträhle, J., Tarish, F., Tanoglidí, A., Vickovic, S., Larsson, L., et al. (2018). Spatial maps of prostate cancer transcriptomes reveal an unexplored landscape of heterogeneity. *Nat. Commun.* 9, 2419. <https://doi.org/10.1038/s41467-018-04724-5>.
27. Gene Ontology Consortium (2021). The Gene Ontology resource: enriching a GOld mine. *Nucleic Acids Res.* 49, D325–d334. <https://doi.org/10.1093/nar/gkaa1113>.
28. Aier, I., Semwal, R., Dhara, A., Sen, N., and Varadwaj, P.K. (2019). An integrated epigenome and transcriptome analysis identifies PAX2 as a master regulator of drug resistance in high grade pancreatic ductal adenocarcinoma. *PLoS One* 14, e0223554. <https://doi.org/10.1371/journal.pone.0223554>.
29. Amrutkar, M., and Gladhaug, I.P. (2017). Pancreatic cancer chemoresistance to gemcitabine. *Cancers* 9, E157. <https://doi.org/10.3390/cancers9110157>.
30. Bailey, P., Chang, D.K., Nones, K., Johns, A.L., Patch, A.M., Gingras, M.C., Miller, D.K., Christ, A.N., Bruxner, T.J.C., Quinn, M.C., et al. (2016). Genomic analyses identify molecular subtypes of pancreatic cancer. *Nature* 531, 47–52. <https://doi.org/10.1038/nature16965>.
31. Chang, Z., Zhang, Y., Liu, J., Guan, C., Gu, X., Yang, Z., Ye, Q., Ding, L., and Liu, R. (2019). GATA1 promotes gemcitabine resistance in pancreatic cancer through antiapoptotic pathway. *J. Oncol.* 2019, 9474273. <https://doi.org/10.1155/2019/9474273>.
32. Collisson, E.A., Sadanandam, A., Olson, P., Gibb, W.J., Truitt, M., Gu, S., Cooc, J., Weinkle, J., Kim, G.E., Jakkula, L., et al. (2011). Subtypes of

- pancreatic ductal adenocarcinoma and their differing responses to therapy. *Nat. Med.* 17, 500–503. <https://doi.org/10.1038/nm.2344>.
33. Drokhyansky, E., Smillie, C.S., Van Wittenberghe, N., Ericsson, M., Griffin, G.K., Eraslan, G., Dionne, D., Cuoco, M.S., Goder-Reiser, M.N., Sharova, T., et al. (2020). The human and mouse enteric nervous system at single-cell resolution. *Cell* 182, 1606–1622.e23. <https://doi.org/10.1016/j.cell.2020.08.003>.
 34. Ebersole, J.L., Novak, M.J., Orraca, L., Martinez-Gonzalez, J., Kirakodu, S., Chen, K.C., Stromberg, A., and Gonzalez, O.A. (2018). Hypoxia-inducible transcription factors, HIF1A and HIF2A, increase in aging mucosal tissues. *Immunology* 154, 452–464. <https://doi.org/10.1111/imm.12894>.
 35. Haber, A.L., Biton, M., Rogel, N., Herbst, R.H., Shekhar, K., Smillie, C., Burgin, G., Delorey, T.M., Howitt, M.R., Katz, Y., et al. (2017). A single-cell survey of the small intestinal epithelium. *Nature* 551, 333–339. <https://doi.org/10.1038/nature24489>.
 36. He, L., Zhu, H., Zhou, S., Wu, T., Wu, H., Yang, H., Mao, H., Sekharkathera, C., Janardhan, A., Edick, A.M., et al. (2018). Wnt pathway is involved in 5-FU drug resistance of colorectal cancer cells. *Exp. Mol. Med.* 50, 1–12. <https://doi.org/10.1038/s12276-018-0128-8>.
 37. Ho, W.J., Jaffee, E.M., and Zheng, L. (2020). The tumour microenvironment in pancreatic cancer - clinical challenges and opportunities. *Nat. Rev. Clin. Oncol.* 17, 527–540. <https://doi.org/10.1038/s41571-020-0363-5>.
 38. James, K.R., Gomes, T., Elmentaite, R., Kumar, N., Gulliver, E.L., King, H.W., Stares, M.D., Bareham, B.R., Ferdinand, J.R., Petrova, V.N., et al. (2020). Distinct microbial and immune niches of the human colon. *Nat. Immunol.* 21, 343–353. <https://doi.org/10.1038/s41590-020-0602-z>.
 39. Kirby, M.K., Ramaker, R.C., Gertz, J., Davis, N.S., Johnston, B.E., Oliver, P.G., Sexton, K.C., Greeno, E.W., Christein, J.D., Heslin, M.J., et al. (2016). RNA sequencing of pancreatic adenocarcinoma tumors yields novel expression patterns associated with long-term survival and reveals a role for ANGPTL4. *Mol. Oncol.* 10, 1169–1182. <https://doi.org/10.1016/j.molonc.2016.05.004>.
 40. Kumar, M.P., Du, J., Lagoudas, G., Jiao, Y., Sawyer, A., Drummond, D.C., Lauffenburger, D.A., and Raue, A. (2018). Analysis of single-cell RNA-seq identifies cell-cell communication associated with tumor characteristics. *Cell Rep.* 25, 1458–1468.e4. <https://doi.org/10.1016/j.celrep.2018.10.047>.
 41. Li, H., Courtois, E.T., Sengupta, D., Tan, Y., Chen, K.H., Goh, J.J.L., Kong, S.L., Chua, C., Hon, L.K., Tan, W.S., et al. (2017). Reference component analysis of single-cell transcriptomes elucidates cellular heterogeneity in human colorectal tumors. *Nat. Genet.* 49, 708–718. <https://doi.org/10.1038/ng.3818>.
 42. Li, Q., O'Malley, M.E., Bartlett, D.L., and Guo, Z.S. (2011). Homeobox gene *Rhox5* is regulated by epigenetic mechanisms in cancer and stem cells and promotes cancer growth. *Mol. Cancer* 10, 63. <https://doi.org/10.1186/1476-4598-10-63>.
 43. Liberzon, A., Birger, C., Thorvaldsdóttir, H., Ghandi, M., Mesirov, J.P., and Tamayo, P. (2015). The Molecular Signatures Database (MSigDB) hallmark gene set collection. *Cell Syst.* 1, 417–425. <https://doi.org/10.1016/j.cels.2015.12.004>.
 44. Moffitt, R.A., Marayati, R., Flate, E.L., Volmar, K.E., Loeza, S.G.H., Hoadley, K.A., Rashid, N.U., Williams, L.A., Eaton, S.C., Chung, A.H., et al. (2015). Virtual microdissection identifies distinct tumor- and stroma-specific subtypes of pancreatic ductal adenocarcinoma. *Nat. Genet.* 47, 1168–1178. <https://doi.org/10.1038/ng.3398>.
 45. Muraro, M.J., Dharmadhikari, G., Grün, D., Groen, N., Dielen, T., Jansen, E., van Gorp, L., Engelse, M.A., Carlotti, F., de Koning, E.J.P., and van Oudenaarden, A. (2016). A single-cell transcriptome atlas of the human pancreas. *Cell Syst.* 3, 385–394.e3. <https://doi.org/10.1016/j.cels.2016.09.002>.
 46. Nagy, Á., Pongor, L.S., Szabó, A., Santarpia, M., and Gyórfy, B. (2017). KRAS driven expression signature has prognostic power superior to mutation status in non-small cell lung cancer. *Int. J. Cancer* 140, 930–937. <https://doi.org/10.1002/ijc.30509>.
 47. Noordhuis, P., Laan, A.C., van de Born, K., Honeywell, R.J., and Peters, G.J. (2019). Coexisting molecular determinants of acquired oxaliplatin resistance in human colorectal and ovarian cancer cell lines. *Int. J. Mol. Sci.* 20, E3619. <https://doi.org/10.3390/ijms20153619>.
 48. Parasido, E., Avetian, G.S., Naeem, A., Graham, G., Pishvaian, M., Glasgow, E., Mudambi, S., Lee, Y., Ihemelandu, C., Choudhry, M., et al. (2019). The sustained induction of c-MYC drives nab-paclitaxel resistance in primary pancreatic ductal carcinoma cells. *Mol. Cancer Res.* 17, 1815–1827. <https://doi.org/10.1158/1541-7786.Mcr-19-0191>.
 49. Pek, M., Yatim, S.M.J.M., Chen, Y., Li, J., Gong, M., Jiang, X., Zhang, F., Zheng, J., Wu, X., and Yu, Q. (2017). Oncogenic KRAS-associated gene signature defines co-targeting of CDK4/6 and MEK as a viable therapeutic strategy in colorectal cancer. *Oncogene* 36, 4975–4986. <https://doi.org/10.1038/ncr.2017.120>.
 50. Peng, J., Sun, B.F., Chen, C.Y., Zhou, J.Y., Chen, Y.S., Chen, H., Liu, L., Huang, D., Jiang, J., Cui, G.S., et al. (2019). Single-cell RNA-seq highlights intra-tumoral heterogeneity and malignant progression in pancreatic ductal adenocarcinoma. *Cell Res.* 29, 725–738. <https://doi.org/10.1038/s41422-019-0195-y>.
 51. Rambow, F., Job, B., Petit, V., Gesbert, F., Delmas, V., Seberg, H., Meurice, G., Van Otterloo, E., Dessen, P., Robert, C., et al. (2015). New functional signatures for understanding melanoma biology from tumor cell lineage-specific analysis. *Cell Rep.* 13, 840–853. <https://doi.org/10.1016/j.celrep.2015.09.037>.
 52. Sehgal, K., Portell, A., Ivanova, E.V., Lizotte, P.H., Mahadevan, N.R., Greene, J.R., Vajdi, A., Gurjao, C., Teceno, T., Taus, L.J., et al. (2021). Dynamic single-cell RNA sequencing identifies immunotherapy persister cells following PD-1 blockade. *J. Clin. Invest.* 131, 135038. <https://doi.org/10.1172/jci135038>.
 53. Sethy, C., and Kundu, C.N. (2021). 5-Fluorouracil (5-FU) resistance and the new strategy to enhance the sensitivity against cancer: implication of DNA repair inhibition. *Biomed. Pharmacother.* 137, 111285. <https://doi.org/10.1016/j.biopha.2021.111285>.
 54. Smillie, C.S., Biton, M., Ordovas-Montanes, J., Sullivan, K.M., Burgin, G., Graham, D.B., Herbst, R.H., Rogel, N., Slyper, M., Waldman, J., et al. (2019). Intra- and inter-cellular rewiring of the human colon during ulcerative colitis. *Cell* 178, 714–730.e22. <https://doi.org/10.1016/j.cell.2019.06.029>.
 55. Tosti, L., Hang, Y., Debnath, O., Tiesmeyer, S., Trefzer, T., Steiger, K., Ten, F.W., Lukassen, S., Ballke, S., Kühl, A.A., et al. (2021). Single-Nucleus and in situ RNA-sequencing reveal cell topographies in the human pancreas. *Gastroenterology* 160, 1330–1344.e11. <https://doi.org/10.1053/j.gastro.2020.11.010>.
 56. Vallo, S., Köpp, R., Michaelis, M., Rothweiler, F., Bartsch, G., Brandt, M.P., Gust, K.M., Wezel, F., Blaheta, R.A., Haferkamp, A., and Cinatl, J., Jr. (2017). Resistance to nanoparticle albumin-bound paclitaxel is mediated by ABCB1 in urothelial cancer cells. *Oncol. Lett.* 13, 4085–4092. <https://doi.org/10.3892/ol.2017.5986>.
 57. Varghese, V., Magnani, L., Harada-Shoji, N., Mauri, F., Szydlowski, R.M., Yao, S., Lam, E.W.F., and Kenny, L.M. (2019). FOXM1 modulates 5-FU resistance in colorectal cancer through regulating TYMS expression. *Sci. Rep.* 9, 1505. <https://doi.org/10.1038/s41598-018-38017-0>.
 58. Watanabe, T., Kobunai, T., Yamamoto, Y., Matsuda, K., Ishihara, S., Nozawa, K., Iinuma, H., Ikeuchi, H., and Eshima, K. (2011). Differential gene expression signatures between colorectal cancers with and without KRAS mutations: crosstalk between the KRAS pathway and other signaling pathways. *Eur. J. Cancer* 47, 1946–1954. <https://doi.org/10.1016/j.ejca.2011.03.029>.
 59. Wu, Z.X., Yang, Y., Zeng, L., Patel, H., Bo, L., Lin, L., and Chen, Z.S. (2020). Establishment and characterization of an irinotecan-resistant human colon cancer cell line. *Front. Oncol.* 10, 624954. <https://doi.org/10.3389/fonc.2020.624954>.

60. Yang, L., Forker, L., Irlam, J.J., Pillay, N., Choudhury, A., and West, C.M.L. (2018). Validation of a hypoxia related gene signature in multiple soft tissue sarcoma cohorts. *Oncotarget* 9, 3946–3955. <https://doi.org/10.18632/oncotarget.23280>.
61. Yuzhalin, A.E., Lim, S.Y., Gordon-Weeks, A.N., Fischer, R., Kessler, B.M., Yu, D., and Muschel, R.J. (2019). Proteomics analysis of the matrixome from MC38 experimental mouse liver metastases. *Am. J. Physiol. Gastrointest. Liver Physiol.* 317, G625–g639. <https://doi.org/10.1152/ajpgi.00014.2019>.
62. Zhang, J., Hu, H., Xu, S., Jiang, H., Zhu, J., Qin, E., He, Z., and Chen, E. (2020). The functional effects of key driver KRAS mutations on gene expression in lung cancer. *Front. Genet.* 11, 17. <https://doi.org/10.3389/fgene.2020.00017>.
63. Ortiz, C., Navarro, J.F., Jurek, A., Märtin, A., Lundeberg, J., and Meletis, K. (2020). Molecular atlas of the adult mouse brain. *Sci. Adv.* 6, eabb3446. <https://doi.org/10.1126/sciadv.abb3446>.
64. Kawai, K., Uemura, M., Munakata, K., Takahashi, H., Haraguchi, N., Nishimura, J., Hata, T., Matsuda, C., Ikenaga, M., Murata, K., et al. (2017). Fructose-bisphosphate aldolase A is a key regulator of hypoxic adaptation in colorectal cancer cells and involved in treatment resistance and poor prognosis. *Int. J. Oncol.* 50, 525–534. <https://doi.org/10.3892/ijco.2016.3814>.
65. Arit, A., and Schäfer, H. (2011). Role of the immediate early response 3 (IER3) gene in cellular stress response, inflammation and tumorigenesis. *Eur. J. Cell Biol.* 90, 545–552. <https://doi.org/10.1016/j.ejcb.2010.10.002>.
66. Anderson, N.M., and Simon, M.C. (2020). The tumor microenvironment. *Curr. Biol.* 30, R921–r925. <https://doi.org/10.1016/j.cub.2020.06.081>.
67. Acerbi, I., Cassereau, L., Dean, I., Shi, Q., Au, A., Park, C., Chen, Y.Y., Liphardt, J., Hwang, E.S., and Weaver, V.M. (2015). Human breast cancer invasion and aggression correlates with ECM stiffening and immune cell infiltration. *Integr. Biol.* 7, 1120–1134. <https://doi.org/10.1039/c5ib00040h>.
68. Jiao, D., Cai, Z., Choksi, S., Ma, D., Choe, M., Kwon, H.J., Baik, J.Y., Rowan, B.G., Liu, C., and Liu, Z.G. (2018). Necroptosis of tumor cells leads to tumor necrosis and promotes tumor metastasis. *Cell Res.* 28, 868–870. <https://doi.org/10.1038/s41422-018-0058-y>.
69. Kim, A.R., Choi, S.J., Park, J., Kwon, M., Chowdhury, T., Yu, H.J., Kim, S., Kang, H., Kim, K.M., Park, S.H., et al. (2022). Spatial immune heterogeneity of hypoxia-induced exhausted features in high-grade glioma. *Oncolmmunology* 11, 2026019. <https://doi.org/10.1080/2162402x.2022.2026019>.
70. Winkler, J., Abisoye-Ogunniyan, A., Metcalf, K.J., and Werb, Z. (2020). Concepts of extracellular matrix remodelling in tumour progression and metastasis. *Nat. Commun.* 11, 5120. <https://doi.org/10.1038/s41467-020-18794-x>.
71. Selby, M.J., Engelhardt, J.J., Johnston, R.J., Lu, L.S., Han, M., Thudium, K., Yao, D., Quigley, M., Valle, J., Wang, C., et al. (2016). Preclinical development of ipilimumab and nivolumab combination immunotherapy: mouse tumor models, in vitro functional studies, and cynomolgus macaque toxicology. *PLoS One* 11, e0161779. <https://doi.org/10.1371/journal.pone.0161779>.
72. Lewis, K.E., Selby, M.J., Masters, G., Valle, J., Dito, G., Curtis, W.R., Garcia, R., Mink, K.A., Waggie, K.S., Holdren, M.S., et al. (2017). Interleukin-21 combined with PD-1 or CTLA-4 blockade enhances antitumor immunity in mouse tumor models. *Oncolmmunology* 7, e1377873. <https://doi.org/10.1080/2162402x.2017.1377873>.
73. Kashyap, A.S., Schmittnaegel, M., Rigamonti, N., Pais-Ferreira, D., Mueller, P., Buchi, M., Ooi, C.H., Kreuzaler, M., Hirschmann, P., Guichard, A., et al. (2020). Optimized antiangiogenic reprogramming of the tumor microenvironment potentiates CD40 immunotherapy. *Proc. Natl. Acad. Sci. USA* 117, 541–551. <https://doi.org/10.1073/pnas.1902145116>.
74. Grieb, G., Kim, B.S., Simons, D., Bernhagen, J., and Pallua, N. (2014). MIF and CD74 - suitability as clinical biomarkers. *Mini Rev. Med. Chem.* 14, 1125–1131. <https://doi.org/10.2174/1389557515666150203143317>.
75. David, J.R. (1966). Delayed hypersensitivity in vitro: its mediation by cell-free substances formed by lymphoid cell-antigen interaction. *Proc. Natl. Acad. Sci. USA* 56, 72–77. <https://doi.org/10.1073/pnas.56.1.72>.
76. Bloom, B.R., and Bennett, B. (1966). Mechanism of a reaction in vitro associated with delayed-type hypersensitivity. *Science* 153, 80–82. <https://doi.org/10.1126/science.153.3731.80>.
77. Taylor, M.A., Hughes, A.M., Walton, J., Coenen-Stass, A.M.L., Magiera, L., Mooney, L., Bell, S., Staniszevska, A.D., Sandin, L.C., Barry, S.T., et al. (2019). Longitudinal immune characterization of syngeneic tumor models to enable model selection for immune oncology drug discovery. *J. Immunother. Cancer* 7, 328. <https://doi.org/10.1186/s40425-019-0794-7>.
78. Bhattacharjee, S., Hamberger, F., Ravichandra, A., Miller, M., Nair, A., Affo, S., Filioli, A., Chin, L., Savage, T.M., Yin, D., et al. (2021). Tumor restriction by type I collagen opposes tumor-promoting effects of cancer-associated fibroblasts. *J. Clin. Invest.* 131, 146987. <https://doi.org/10.1172/jci146987>.
79. Wang, X.Q., Tang, Z.X., Yu, D., Cui, S.J., Jiang, Y.H., Zhang, Q., Wang, J., Yang, P.Y., and Liu, F. (2016). Epithelial but not stromal expression of collagen alpha-1(III) is a diagnostic and prognostic indicator of colorectal carcinoma. *Oncotarget* 7, 8823–8838. <https://doi.org/10.18632/oncotarget.6815>.
80. Arlauckas, S.P., Garren, S.B., Garris, C.S., Kohler, R.H., Oh, J., Pittet, M.J., and Weissleder, R. (2018). Arg1 expression defines immunosuppressive subsets of tumor-associated macrophages. *Theranostics* 8, 5842–5854. <https://doi.org/10.7150/thno.26888>.
81. Wang, W., Knovich, M.A., Coffman, L.G., Torti, F.M., and Torti, S.V. (2010). Serum ferritin: past, present and future. *Biochim. Biophys. Acta* 1800, 760–769. <https://doi.org/10.1016/j.bbagen.2010.03.011>.
82. Hwang, W.L., Jagadeesh, K.A., Guo, J.A., Hoffman, H.I., Yadollahpour, P., Mohan, R., Drokhlyansky, E., Van Wittenbergh, N., Ashenberg, O., Farhi, S., et al. (2020). Single-nucleus and spatial transcriptomics of archival pancreatic cancer reveals multi-compartment reprogramming after neoadjuvant treatment. Preprint at bioRxiv. <https://doi.org/10.1101/2020.08.25.267336>.
83. Baghban, R., Roshangar, L., Jahanban-Esfahlan, R., Seidi, K., Ebrahimi-Kalan, A., Jaymand, M., Kolahian, S., Javaheri, T., and Zare, P. (2020). Tumor microenvironment complexity and therapeutic implications at a glance. *Cell Commun. Signal.* 18, 59. <https://doi.org/10.1186/s12964-020-0530-4>.
84. Brady, L., Kriner, M., Coleman, I., Morrissey, C., Roudier, M., True, L.D., Gulati, R., Plymate, S.R., Zhou, Z., Birditt, B., et al. (2021). Inter- and intra-tumor heterogeneity of metastatic prostate cancer determined by digital spatial gene expression profiling. *Nat. Commun.* 12, 1426. <https://doi.org/10.1038/s41467-021-21615-4>.
85. Henke, E., Nandigama, R., and Ergün, S. (2019). Extracellular matrix in the tumor microenvironment and its impact on cancer therapy. *Front. Mol. Biosci.* 6, 160. <https://doi.org/10.3389/fmolb.2019.00160>.
86. Li, J., Chekkoury, A., Prakash, J., Glasl, S., Vetschera, P., Koberstein-Schwarz, B., Olefir, I., Gujrati, V., Omar, M., and Ntziachristos, V. (2020). Spatial heterogeneity of oxygenation and haemodynamics in breast cancer resolved in vivo by conical multispectral optoacoustic mesoscopy. *Light Sci. Appl.* 9, 57. <https://doi.org/10.1038/s41377-020-0295-y>.
87. Collisson, E.A., Bailey, P., Chang, D.K., and Biankin, A.V. (2019). Molecular subtypes of pancreatic cancer. *Nat. Rev. Gastroenterol. Hepatol.* 16, 207–220. <https://doi.org/10.1038/s41575-019-0109-y>.
88. Wen, Y., Cai, W., Yang, J., Fu, X., Putha, L., Xia, Q., Windsor, J.A., Phillips, A.R., Tyndall, J.D.A., Du, D., et al. (2021). Targeting macrophage migration inhibitory factor in acute pancreatitis and pancreatic cancer. *Front. Pharmacol.* 12, 638950. <https://doi.org/10.3389/fphar.2021.638950>.
89. Ahmed, A., Köhler, S., Klotz, R., Giese, N., Lasitschka, F., Hackert, T., Springfield, C., Zörnig, I., Jäger, D., and Halama, N. (2021). Peripheral

- blood and tissue assessment highlights differential tumor-circulatory gradients of IL2 and MIF with prognostic significance in resectable pancreatic ductal adenocarcinoma. *Oncolmmunology* 10, 1962135. <https://doi.org/10.1080/2162402X.2021.1962135>.
90. Mahalingam, D., Patel, M.R., Sachdev, J.C., Hart, L.L., Halama, N., Ramanathan, R.K., Sarantopoulos, J., Völkel, D., Youssef, A., de Jong, F.A., and Tsimberidou, A.M. (2020). Phase I study of imalumab (BAX69), a fully human recombinant antioxidantized macrophage migration inhibitory factor antibody in advanced solid tumours. *Br. J. Clin. Pharmacol.* 86, 1836–1848. <https://doi.org/10.1111/bcp.14289>.
 91. Kim, H.K., Bhattarai, K.R., Junjappa, R.P., Ahn, J.H., Pagire, S.H., Yoo, H.J., Han, J., Lee, D., Kim, K.W., Kim, H.R., and Chae, H.J. (2020). TMBIM6/BI-1 contributes to cancer progression through assembly with mTORC2 and AKT activation. *Nat. Commun.* 11, 4012. <https://doi.org/10.1038/s41467-020-17802-4>.
 92. Ramilowski, J.A., Goldberg, T., Harshbarger, J., Kloppmann, E., Kloppman, E., Lizio, M., Satagopam, V.P., Itoh, M., Kawaji, H., Carninci, P., et al. (2015). A draft network of ligand-receptor-mediated multicellular signalling in human. *Nat. Commun.* 6, 7866. <https://doi.org/10.1038/ncomms8866>.
 93. Islam, S., Kitagawa, T., Baron, B., Abiko, Y., Chiba, I., and Kuramitsu, Y. (2021). ITGA2, LAMB3, and LAMC2 may be the potential therapeutic targets in pancreatic ductal adenocarcinoma: an integrated bioinformatics analysis. *Sci. Rep.* 11, 10563. <https://doi.org/10.1038/s41598-021-90077-x>.
 94. Sleightholm, R.L., Neilsen, B.K., Li, J., Steele, M.M., Singh, R.K., Hollingsworth, M.A., and Oupicky, D. (2017). Emerging roles of the CXCL12/CXCR4 axis in pancreatic cancer progression and therapy. *Pharmacol. Ther.* 179, 158–170. <https://doi.org/10.1016/j.pharmthera.2017.05.012>.
 95. Portella, L., Bello, A.M., and Scala, S. (2021). CXCL12 signaling in the tumor microenvironment. *Adv. Exp. Med. Biol.* 1302, 51–70. https://doi.org/10.1007/978-3-030-62658-7_5.
 96. Jayasingam, S.D., Citartan, M., Thang, T.H., Mat Zin, A.A., Ang, K.C., and Ch'ng, E.S. (2019). Evaluating the polarization of tumor-associated macrophages into M1 and M2 phenotypes in human cancer tissue: technicalities and challenges in routine clinical practice. *Front. Oncol.* 9, 1512. <https://doi.org/10.3389/fonc.2019.01512>.
 97. He, B., Bergensträhle, L., Stenbeck, L., Abid, A., Andersson, A., Borg, Å., Maaskola, J., Lundeberg, J., and Zou, J. (2020). Integrating spatial gene expression and breast tumour morphology via deep learning. *Nat. Biomed. Eng.* 4, 827–834. <https://doi.org/10.1038/s41551-020-0578-x>.
 98. Lohoff, T., Ghazanfar, S., Missarova, A., Koulou, N., Pierson, N., Griffiths, J.A., Bardot, E.S., Eng, C.H.L., Tyser, R.C.V., Argelaguet, R., et al. (2022). Integration of spatial and single-cell transcriptomic data elucidates mouse organogenesis. *Nat. Biotechnol.* 40, 74–85. <https://doi.org/10.1038/s41587-021-01006-2>.
 99. Ye, L., Liu, Y., Zhu, X., Duan, T., Wang, C., Fu, X., Song, P., Yuan, S., Liu, H., Sun, L., et al. (2022). Digital spatial profiling of individual glomeruli from patients with anti-neutrophil cytoplasmic autoantibody-associated glomerulonephritis. *Front. Immunol.* 13, 831253. <https://doi.org/10.3389/fimmu.2022.831253>.
 100. Biancalani, T., Scalia, G., Buffoni, L., Avasthi, R., Lu, Z., Sanger, A., Tokcan, N., Vanderburg, C.R., Segerstolpe, Å., Zhang, M., et al. (2021). Deep learning and alignment of spatially resolved single-cell transcriptomes with Tangram. *Nat. Methods* 18, 1352–1362. <https://doi.org/10.1038/s41592-021-01264-7>.
 101. Ma, Y., and Zhou, X. (2022). Spatially informed cell-type deconvolution for spatial transcriptomics. *Nat. Biotechnol.* 40, 1349–1359. <https://doi.org/10.1038/s41587-022-01273-7>.
 102. Li, B., Zhang, W., Guo, C., Xu, H., Li, L., Fang, M., Hu, Y., Zhang, X., Yao, X., Tang, M., et al. (2022). Benchmarking spatial and single-cell transcriptomics integration methods for transcript distribution prediction and cell type deconvolution. *Nat. Methods* 19, 662–670. <https://doi.org/10.1038/s41592-022-01480-9>.
 103. Shengquan, C., Boheng, Z., Xiaoyang, C., Xuegong, Z., and Rui, J. (2021). stPlus: a reference-based method for the accurate enhancement of spatial transcriptomics. *Bioinformatics* 37 (Suppl_1), i299–i307. <https://doi.org/10.1093/bioinformatics/btab298>.
 104. Yang, Y., Shi, X., Liu, W., Zhou, Q., Chan Lau, M., Chun Tatt Lim, J., Sun, L., Ng, C.C.Y., Yeong, J., and Liu, J. (2022). SC-MEB: Spatial clustering with hidden Markov random field using empirical Bayes. *Brief. Bioinform.* 23, bbab466. <https://doi.org/10.1093/bib/bbab466>.
 105. Zhao, E., Stone, M.R., Ren, X., Guenthoer, J., Smythe, K.S., Pulliam, T., Williams, S.R., Uyttingco, C.R., Taylor, S.E.B., Nghiem, P., et al. (2021). Spatial transcriptomics at subspot resolution with BayesSpace. *Nat. Biotechnol.* 39, 1375–1384. <https://doi.org/10.1038/s41587-021-00935-2>.
 106. Battle, E., and Clevers, H. (2017). Cancer stem cells revisited. *Nat. Med.* 23, 1124–1134. <https://doi.org/10.1038/nm.4409>.
 107. Chan-Seng-Yue, M., Kim, J.C., Wilson, G.W., Ng, K., Figueroa, E.F., O’Kane, G.M., Connor, A.A., Denroche, R.E., Grant, R.C., McLeod, J., et al. (2020). Transcription phenotypes of pancreatic cancer are driven by genomic events during tumor evolution. *Nat. Genet.* 52, 231–240. <https://doi.org/10.1038/s41588-019-0566-9>.
 108. Orth, M., Metzger, P., Gerum, S., Mayerle, J., Schneider, G., Belka, C., Schnurr, M., and Lauber, K. (2019). Pancreatic ductal adenocarcinoma: biological hallmarks, current status, and future perspectives of combined modality treatment approaches. *Radiat. Oncol.* 14, 141. <https://doi.org/10.1186/s13014-019-1345-6>.
 109. Zhu, L., Jiang, M., Wang, H., Sun, H., Zhu, J., Zhao, W., Fang, Q., Yu, J., Chen, P., Wu, S., et al. (2021). A narrative review of tumor heterogeneity and challenges to tumor drug therapy. *Ann. Transl. Med.* 9, 1351. <https://doi.org/10.21037/atm-21-1948>.
 110. Lee, S.Y., Ju, M.K., Jeon, H.M., Jeong, E.K., Lee, Y.J., Kim, C.H., Park, H.G., Han, S.I., and Kang, H.S. (2018). Regulation of tumor progression by programmed necrosis. *Oxid. Med. Cell. Longev.* 2018, 3537471. <https://doi.org/10.1155/2018/3537471>.
 111. Hao, Y., Hao, S., Andersen-Nissen, E., Mauck, W.M., 3rd, Zheng, S., Butler, A., Lee, M.J., Wilk, A.J., Darby, C., Zager, M., et al. (2021). Integrated analysis of multimodal single-cell data. *Cell* 184, 3573–3587.e29. <https://doi.org/10.1016/j.cell.2021.04.048>.
 112. Pebesma, E.J., Gomez-Rubio, V., and Bivand, R. (2013). *Applied Spatial Data Analysis with R, Second edition* (Springer).
 113. Csárdi, G.N.T. (2006). The Igraph Software Package for Complex Network Research (InterJournal Complex Systems), p. 1695. <https://doi.org/10.5281/zenodo.3630268>.
 114. Baddeley, A., Rubak, E., and Turner, R. (2015). *Spatial Point Patterns: Methodology and Applications with R*. 2015 (London: Chapman and Hall/CRC Press).
 115. Szklarczyk, D., Gable, A.L., Lyon, D., Junge, A., Wyder, S., Huerta-Cepas, J., Simonovic, M., Doncheva, N.T., Morris, J.H., Bork, P., et al. (2019). STRING v11: protein-protein association networks with increased coverage, supporting functional discovery in genome-wide experimental datasets. *Nucleic Acids Res.* 47, D607–D613. <https://doi.org/10.1093/nar/gky1131>.
 116. Zappia, L., and Oshlack, A. (2018). Clustering trees: a visualization for evaluating clusterings at multiple resolutions. *GigaScience* 7. <https://doi.org/10.1093/gigascience/giy083>.
 117. Finak, G., McDavid, A., Yajima, M., Deng, J., Gersuk, V., Shalek, A.K., Slichter, C.K., Miller, H.W., McElrath, M.J., Pric, M., et al. (2015). MAST: a flexible statistical framework for assessing transcriptional changes and characterizing heterogeneity in single-cell RNA sequencing data. *Genome Biol.* 16, 278. <https://doi.org/10.1186/s13059-015-0844-5>.
 118. Brett, C.N., Neuhaus, I., Inberg, G., Ali, M., and Squibb, B.M. (2021). *Periscope: Enterprise Streamlined 'Shiny' Application Framework*.

119. Neuhaus, I.B., and Brett, C.N. (2021). *canvasXpress: Visualization Package for CanvasXpress in R*.
120. Villacampa, E.G., Larsson, L., Kvastad, L., Andersson, A., Carlson, J., and Lundeberg, J. (2020). Genome-wide spatial expression profiling in FFPE tissues. Preprint at bioRxiv. <https://doi.org/10.1101/2020.07.24.219758>.
121. Deng, J., Dong, W., Socher, R., Li, L.J., Li, K., and Fei-Fei, L. (2009). ImageNet: a large-scale hierarchical image database. In IEEE Conference on Computer Vision and Pattern Recognition, pp. 248–255. <https://doi.org/10.1109/CVPR.2009.5206848>.
122. Huang, G.L., Liu, Z., Van Der Maaten, L., and Weinberger, K.Q. (2017). Densely connected convolutional networks. In 2017 IEEE Conference on Computer Vision and Pattern Recognition (CVPR), pp. 2261–2269. <https://doi.org/10.1109/CVPR.2017.243>.
123. Janowczyk, A., and Madabhushi, A. (2016). Deep learning for digital pathology image analysis: a comprehensive tutorial with selected use cases. *J. Pathol. Inform.* 7, 29. <https://doi.org/10.4103/2153-3539.186902>.
124. He, K.Z., Zhang, X., Ren, S., and Sun, J. (2016). Deep residual learning for image recognition. In 2016 IEEE Conference on Computer Vision and Pattern Recognition (CVPR), pp. 770–778. <https://doi.org/10.1109/CVPR.2016.90>.
125. Stuart, T., Butler, A., Hoffman, P., Hafemeister, C., Papalexi, E., Mauck, W.M., 3rd, Hao, Y., Stoeckius, M., Smibert, P., and Satija, R. (2019). Comprehensive integration of single-cell data. *Cell* 177, 1888–1902.e21. <https://doi.org/10.1016/j.cell.2019.05.031>.
126. Hafemeister, C., and Satija, R. (2019). Normalization and variance stabilization of single-cell RNA-seq data using regularized negative binomial regression. *Genome Biol.* 20, 296. <https://doi.org/10.1186/s13059-019-1874-1>.
127. Tirosh, I., Izar, B., Prakadan, S.M., Wadsworth, M.H., 2nd, Treacy, D., Trombetta, J.J., Rotem, A., Rodman, C., Lian, C., Murphy, G., et al. (2016). Dissecting the multicellular ecosystem of metastatic melanoma by single-cell RNA-seq. *Science* 352, 189–196. <https://doi.org/10.1126/science.aad0501>.
128. Haynes, W. (2013). Bonferroni correction. In *Encyclopedia of Systems Biology*, W.W. Dubitzky, O. Wolkenhauer, K.H. Cho, and H. Yokota, eds. (Springer). https://doi.org/10.1007/978-1-4419-9863-7_1213.
129. Eraslan, G., Drokhlyansky, E., Anand, S., Fiskin, E., Subramanian, A., Slyper, M., Wang, J., Van Wittenberghe, N., Rouhana, J.M., Waldman, J., et al. (2022). Single-nucleus cross-tissue molecular reference maps toward understanding disease gene function. *Science* 376, eabl4290. <https://doi.org/10.1126/science.abl4290>.

STAR★METHODS

KEY RESOURCES TABLE

REAGENT or RESOURCE	SOURCE	IDENTIFIER
Biological samples		
Human resected PDAC tumor	BioIVT	N/A
Human resected PDAC tumors	Discovery Life Sciences	N/A
B16F10 subcutaneous tumors	BMS	N/A
MC38 subcutaneous tumors	BMS	N/A
Rat colons	BMS	N/A
Chemicals, peptides, and recombinant proteins		
TissueTek O.C.T. Compound	VWR	Cat# 25608-930
Critical commercial assays		
RNA ScreenTape	Agilent	Cat# 5067-5576
RNA ScreenTape Ladder	Agilent	Cat# 5067-5578
RNA ScreenTape Sample Buffer	Agilent	Cat# 5067-5577
Visium Spatial Tissue Optimization Slide & Reagents Kit, 4 samples	10X Genomics	Cat# 1000193
Visium Spatial Gene Expression Slide & Reagents Kit, 16 rxns	10X Genomics	Cat# 1000184
Visium Spatial for FFPE Gene Expression Kit, Human Transcriptome, 16 rxns	10X Genomics	Cat# 1000336
NextSeq 500/550 High Output Kit v2.5 (150 Cycles)	Illumina	Cat# 20024907
NovaSeq 6000 S2 Reagent Kit v1.5 (200 cycles)	Illumina	Cat# 20028315
Deposited data		
Raw and analyzed sequencing data	This paper	GEO: GSE211895
Code and data for BMS Spatial Portal	This paper	GitHub: https://github.com/anvaly/SpatialPortal ; Zenodo: https://doi.org/10.5281/zenodo.7217463
Experimental models: Cell lines		
Mouse: B16F10 cell line	ATCC	Cat# CRL-6475; RRID: CVCL_0159
Mouse: MC38 cell line	MD Anderson Cancer Center, TX	RRID: CVCL_B288
Experimental models: Organisms/strains		
Mice, C57BL/6 (female aged 7–8 weeks)	Charles River	RRID: IMSR_JAX:000,664
Rats, Sprague-Dawley (male aged 6–8 weeks)	Charles River	RRID: MGI:5651135
Software and algorithms		
SpaceRanger-1.2.1	10X Genomics	N/A
R-4.0.3	The R Foundation	https://www.r-project.org/
Seurat-4.0.0	Hao et al., 2021 ¹¹¹	https://satijalab.org/seurat/
spdep-1.1-5	Bivand, 2013 ¹¹²	https://github.com/r-spatial/spdep
igraph-1.2.6	Csárdi, 2006 ¹¹³	https://igraph.org/r/
spatstat-1.64-1	Baddeley, 2015 ¹¹⁴	https://spatstat.org/
STRING	Szklarczyk et al., 2019 ¹¹⁵	https://string-db.org/
clustree-0.4.3	Zappia and Oshlack, 2018 ¹¹⁶	https://github.com/lazappi/clustree
MAST	Finak et al., 2015 ¹¹⁷	https://rglab.github.io/MAST/
Periscope	Brett, 2021 ¹¹⁸	https://periscopeapps.org/
canvasXpress	Neuhaus, 2021 ¹¹⁹	https://github.com/neuhausi/canvasXpress
HALO v3.2.1851.484	Indica Labs	https://indicalab.com/halo

(Continued on next page)

Continued

REAGENT or RESOURCE	SOURCE	IDENTIFIER
BMS Spatial Portal	This paper	http://periscopeapps.org:3838/spatial_portal/
Other		
Zeiss Axio Observer 7 microscope	Zeiss	Cat# 4310079904
LD Plan-Neofluar 20X/0.4na objective	Zeiss	Cat# 4213519972
Plan-Apochromat 20X/0.8na objective	Zeiss	Cat# 4406409903
Plan-Apochromat 10X/0.45na objective	Zeiss	Cat# 4206419910
Axiocam 506 color camera	Zeiss	Cat# 426556
Axiocam 506 mono camera	Zeiss	Cat# 426557
Plan-Apochromat 10X/0.45na objective	Zeiss	Cat# 4230529720
Zeiss filter set 20 HE	Zeiss	Cat# 489020000
4200 TapeStation System	Agilent	Cat# G2991BA
C1000 Touch Thermal Cycler with 96-Deep Well Reaction Module	Bio-Rad	Cat# 1851197

RESOURCE AVAILABILITY

Lead contact

Further information and requests for resources and reagents should be directed to the lead contact, Eugene Drokhyansky (eugene.drokhyansky@bms.com).

Materials availability

This study did not generate new unique reagents.

Data and code availability

- ST images and data have been deposited at GEO and is publicly available as of the date of publication (GEO: GSE211895). Follow-up requests can be made to the [corresponding author](#).
- Original code and data for the BMS Spatial portal has been deposited at GitHub: <https://github.com/anvaly/SpatialPortal> and is publicly available as of the date of publication. DOIs are listed in the [key resources table](#).
- Any additional information required to reanalyze the data reported in this paper is available from the [lead contact](#) upon request.

EXPERIMENTAL MODEL AND SUBJECT DETAILS

Rats

Rats were 6-8-week-old male Sprague-Dawley rats (Charles River Laboratories, CD-SD-001, RRID MGI:5651135). All rat work was performed in accordance with the Institutional Animal Care and Use Committees (IACUC) relevant guidelines at Charles River Laboratories and Bristol Myers Squibb under protocol number CR-0063.

Mice

Mice were 7-8-week-old female C57BL/6 mice (RRID IMSR_JAX:000,664). All mouse work was performed in accordance with the Institutional Animal Care and Use Committees (IACUC) relevant guidelines at Charles River Laboratories and Bristol Myers Squibb under protocol number CR-0067.

B16F10 cell line

B16F10 murine melanoma cells (CRL-6475, RRID CVCL_0159, ATCC) were originally derived from male C57BL/6 mice (RRID IMSR_JAX:000,664).

MC38 cell line

MC38 murine colon adenocarcinoma cells (RRID CVCL_B288, from Dr. James Allison, MD Anderson Cancer Center, TX) were originally derived from female C57BL/6 mice (RRID CVCL_B288).

Human resected PDAC tumors

All tumor resection samples were obtained with informed consent via BioIVT and Discovery Life Sciences. Donor-A tumor was supplied by BioIVT. Donor-B and Donor-C tissues were supplied by Discovery Life Sciences. Age, gender, and other donor metadata were not provided.

METHOD DETAILS

Syngeneic tumor growth

Syngeneic tumors were grown by implanting 1×10^6 or 1.5×10^6 B16F10 (RRID IMSR_JAX:000664) or MC38 (RRID CVCL_B288) cells, respectively, into the flank of female C57BL/6 mice (RRID IMSR_JAX:000664).

Rat colon collection

Rat colons were collected from per CRADL client protocol CR-0063. Following collection, each colon was rinsed with ice-cold PBS and stored in PBS on ice until O.C.T. or FFPE embedding.

Syngeneic mouse tumor collection

Tumors were collected at 10 or 16 days post-implantation. Following collection, each tumor was stored in PBS on ice until O.C.T. embedding. All mouse work was performed in accordance with the Institutional Animal Care and Use Committees (IACUC) relevant guidelines at Charles River Laboratories and Bristol Myers Squibb under protocol number CR-0067.

Fresh-frozen tissue embedding

Tissues were placed in cryomolds with ice-cold TissueTek O.C.T. Compound (VWR, 25608-930) on a pre-cooled aluminum block that was placed in a dry ice and ethanol mixture. Additional O.C.T. was added to ensure the entire tissue was covered. Blocks were stored sealed at -80°C .

FFPE tissue embedding

Tissue was placed in 10% Neutral Buffered Formalin for 24-h fixation. Tissue was then processed for paraffin embedding in a Sakura VIP automated system with vacuum/pressure cycles, dehydrating in graded alcohols to xylene and then paraffin, and embedded into blocks for sectioning.

FFPE block DV200 evaluation

FFPE tissue RNA DV200 scores were evaluated prior to use as described in the Visium Spatial Gene Expression for FFPE – Tissue Preparation Guide (10X Genomics, CG000408 Rev A) with the following modification. RNA was run on an Agilent RNA ScreenTape (Agilent 5067-5576), and DV200 scores were then calculated as the percent of the RNA sample above 200 bases in length, as determined using the Agilent TapeStation Analysis software.

Fresh-frozen histology

Frozen sections were collected on gene expression slides (10X Genomics, PN 2000233) or tissue optimization slides (10X Genomics, PN 3000394) according to manufacturer protocols (10X Genomics, CG000240 RevD). Slides were kept in 50 mL conical tubes at -80°C for no more than a week before staining and processing.

FFPE histology

FFPE sections were collected on gene expression slides (10X Genomics, PN 2000233) or tissue optimization slides (10X Genomics, PN 3000394) and dried at 42°C according to manufacturer protocols (10X Genomics, CG000408 RevA) with the following modification. Sections collected for the polyA-capture protocol were cut at $10 \mu\text{m}$ instead of $5 \mu\text{m}$, as described in Villacampa et al.¹²⁰ Sections collected for the polyA-capture protocol were stored in sealed 50 mL conical tubes at 4°C for no more than 24 h before staining and processing as described in Villacampa et al.¹²⁰ Sections collected for the probe-based protocol were stored in a desiccator overnight at room temperature before staining and processing.

ST section staining and library prep

For fresh-frozen polyA capture ST, sections on gene expression slides (10X Genomics, PN 2000233) or tissue optimization slides (10X Genomics, PN 3000394) were methanol fixed and stained according to the manufacturer protocols (10X Genomics, CG000160 Rev A), and imaged as described below. Sections were imaged with or without a coverslip mounted and removed according to manufacturer protocols (10X Genomics, CG000160 Rev A). Tissue optimization was conducted according to the Visium Tissue Optimization user guide (10X Genomics, CG000238 Rev D). ST libraries were prepared using Visium Spatial Gene Expression reagents (10X Genomics, 1000184) according to the manufacturer user guide (10X Genomics, CG000239 Rev C), using a permeabilization time of 30 and 24 min for rat colon and syngeneic tumors, respectively, as determined during tissue optimization.

For FFPE polyA capture ST, sections collected on gene expression slides (10X Genomics, PN 2000233) or tissue optimization slides (10X Genomics, PN 3000394) were dried, deparaffinized, stained, and coverslipped as described by Villacampa et al.,¹²⁰ and imaged as described below. Decrosslinking was performed as described by Villacampa et al.,¹²⁰ and tissue optimization was performed for Donor-A-FFPE using the Visium Tissue Optimization reagents (10X Genomics, 1000193) and user guide (10X Genomics, CG000238 Rev D) with the following modifications. Permeabilization was tested for 30 and 60 min, using 1X, 2X, and 4X permeabilization enzyme (each tube of permeabilization enzyme, 10X Genomics PN 2000214, was reconstituted in 300 μ L of 0.1 N HCl to make a 4X stock, which was diluted in 0.1 N HCl to create 2X and 1X enzyme solutions). Following tissue removal, tissue optimization slides were imaged as described below. ST libraries were prepared using Visium Spatial Gene Expression reagents (10X Genomics, 1000184) according to the protocol described in Villacampa et al.¹²⁰ with a modified permeabilization (2X permeabilization enzyme for 60 min, as determined during tissue optimization).

For FFPE probe-based ST, sections collected on gene expression slides (10X Genomics, PN 2000233), were dried, deparaffinized, and stained and coverslipped according to manufacturer protocols (10X Genomics, CG000409 Rev A), and imaged as described below. ST libraries were prepared using Visium Spatial for FFPE reagents for the human transcriptome (10X Genomics, 1000336), according to manufacturer protocols (10X Genomics, CG000407 Rev A).

ST chemistry, use of a coverslip, library statistics, and cell number per spot for each sample can be found below, samples in bold are included in the BMS spatial portal (see additional resources for more details):

Sample	ST Protocol	Coverslip	Spots Under Tissue	UMIs per spot, mean	Genes per spot, mean	Mitoch. content, mean	Ribo. content, mean	Cell number, mean	Cell number, SD
Rat Colon									
RatColon_FF_A_e4	FF-polyA	N	1428	13054	3577	6.7%	9.8%	24	12
RatColon_FF_B_e4	FF-polyA	N	1375	14202	3711	6.5%	9.8%	24	12
RatColon_FF_wCS_C_e4	FF-polyA	Y	1453	21526	4580	6.9%	9.4%	29	15
RatColon_FF_wCS_D_e4	FF-polyA	Y	1416	14801	3556	8.9%	10.5%	28	16
RatColon_FFPE_A_e3	FFPE-polyA	N	1393	7144	2448	13.7%	5.8%	N/A	N/A
RatColon_FFPE_C_e3	FFPE-polyA	N	1138	5688	1937	15.9%	5.6%	N/A	N/A
RatColon_FFPE_D_e3	FFPE-polyA	N	1150	7656	2525	15.3%	6.1%	N/A	N/A
RatColon_FF_A_e2	FF-polyA	N	1302	13410	3493	8.4%	7.9%	N/A	N/A
RatColon_FF_B_e2	FF-polyA	N	1286	12841	3454	7.8%	8.6%	N/A	N/A
RatColon_FF_C_e2	FF-polyA	N	1372	10780	3078	8.7%	7.9%	N/A	N/A
RatColon_FF_D_e2	FF-polyA	N	1124	9407	2950	7.3%	7.7%	N/A	N/A
RatColon_FF_A_e1	FF-polyA	N	1276	15875	3575	9.2%	12.3%	N/A	N/A
RatColon_FF_B_e1	FF-polyA	N	1345	16041	3660	9.0%	11.9%	N/A	N/A
RatColon_FF_C_e1	FF-polyA	N	1299	15688	3759	8.2%	12.4%	N/A	N/A
RatColon_FF_D_e1	FF-polyA	N	1388	16971	3673	10.7%	12.4%	N/A	N/A
Human PDAC									
DonorA_FF-pA_A	FF-polyA	N	2754	7149	2815	8.2%	12.1%	12	6
DonorA_FF-pA_B	FF-polyA	N	2802	7299	2950	6.3%	12.0%	14	6
DonorA_FF-pA_C	FF-polyA	N	2064	5346	2383	4.6%	10.6%	14	6
DonorA_FF-pA_D	FF-polyA	N	2860	3804	1877	6.3%	10.8%	13	6
DonorA_FFPE-pA_A	FFPE-polyA	N	2695	2185	869	2.5%	6.9%	20	8
DonorA_FFPE-pA_B	FFPE-polyA	N	2494	1391	589	2.6%	6.8%	21	9
DonorA_FFPE-pA_C	FFPE-polyA	N	2204	1660	681	2.4%	6.8%	22	8
DonorA_FFPE-pA_D	FFPE-polyA	N	3064	1459	734	3.3%	7.3%	14	7
DonorA_FFPE-pA_E	FFPE-polyA	Y	2174	1630	899	1.9%	6.0%	19	10
DonorA_FFPE-probes	FFPE-probes	Y	2197	31044	7265	N/A	N/A	15	8
DonorB_FFPE-probes	FFPE-probes	Y	3164	3817	1677	N/A	N/A	16	9
DonorC_FFPE-probes	FFPE-probes	Y	2258	2361	1248	N/A	N/A	16	10

(Continued on next page)

Continued

Sample	ST Protocol	Coverslip	Spots Under Tissue	UMIs per spot, mean	Genes per spot, mean	Mitocho. content, mean	Ribo. content, mean	Cell number, mean	Cell number, SD
Mouse B16 Syngeneic Tumor									
B16_d10_m1_C_e2	FF-polyA	Y	1469	26714	4998	1.0%	22.1%	21	7
B16_d10_m1_D1_e1	FF-polyA	N	2421	5238	2111	2.6%	15.9%	19	5
B16_d10_m1_D2_e1	FF-polyA	N	2421	17216	4208	2.8%	18.2%	16	5
B16_d16_m2_C_e2	FF-polyA	Y	2188	40375	5196	0.9%	30.9%	18	8
B16_d16_m3_A_e3	FF-polyA	Y	2897	20993	4596	0.5%	22.9%	20	8
B16_d16_m3_C_e3	FF-polyA	Y	3090	22080	4489	1.1%	24.2%	21	9
B16_d16_m4_C_e3	FF-polyA	Y	3444	13143	3747	1.0%	18.3%	18	7
Mouse MC38 Syngeneic Tumor									
MC38_d10_m5_C1_e1	FF-polyA	N	1378	10424	3659	2.4%	17.6%	26	9
MC38_d10_m5_C2_e1	FF-polyA	N	1378	9116	3333	2.1%	17.7%	21	12
MC38_d10_m5_D_e2	FF-polyA	Y	1372	22339	4836	1.4%	23.2%	29	8
MC38_d16_m6_D_e2	FF-polyA	Y	1982	41686	5913	0.9%	31.6%	23	7
MC38_d16_m7_D_e3	FF-polyA	Y	1909	31854	5710	0.7%	26.7%	30	8
MC38_d16_m8_D_e3	FF-polyA	Y	3600	14341	3834	0.9%	24.6%	26	7

Imaging

Following H&E staining, slides were imaged using a Zeiss Axio Observer 7 microscope (Zeiss, 4310079904) with an Axiocam 506 color camera (Zeiss, 426556). For gene expression slides (10X Genomics, PN 2000233), stained sections without coverslips were imaged using an LD Plan-Neofluar 20X/0.4na objective (Zeiss, 4213519972) and stained sections with coverslips were imaged with a Plan-Apochromat 20X/0.8na objective (Zeiss, 4406409903). For tissue optimization slides (10X Genomics, PN 3000394), stained sections were imaged with a Plan-Apochromat 10X/0.45na objective (Zeiss, 4206419910). Following tissue removal, fluorescence imaging of tissue optimization slides was performed with the same microscope, using an Axiocam 506 mono camera (Zeiss, 426557), Plan-Apochromat 10X/0.45na objective (Zeiss, 4206419910), Solid-state light source Colibri 7, type RYB-UV light source (Zeiss, 4230529720), and the Zeiss filter set 20 HE (Zeiss, 489020000).

Sequencing

All ST libraries were sequenced according to manufacturer protocols (10X Genomics, CG000238 Rev D and CG000407 Rev A for polyA-capture and probe-based libraries, respectively). PolyA-capture ST libraries were sequenced on either the Illumina NextSeq 500/550 High Output v2.5 flowcells (Illumina, 20024907) or the Illumina NovaSeq 6000 S2 v1.5 (Illumina, 20028315). Probe-based ST libraries were sequenced at 10X Genomics on the NovaSeq 6000 according to manufacturer protocols (10X Genomics, CG000409 Rev A), with a read 2 length of 90 cycles.

Digital pathology deep learning model development

Whole-slide images were loaded into HALO v3.2.1851.484 (Indica Labs) on an AWS EC2 instance g4dn.4xlarge equipped with an NVIDIA Tesla T4 graphics card.

Convolutional neural networks pretrained for image analysis tasks^{121,122} were adapted to experiment-specific tasks via transfer learning. To generate training data (e.g., ground truth annotations) for the transfer learning, the images were first reviewed by the image analyst and pathologist to identify the salient (morphologically/visually distinct) features present. The sample cohorts are relatively small in the context of deep learning, so care was taken to limit the number of classes to maximize the dissimilarity in image features/textures between classes¹²³ while still providing meaningful orthogonal validation of genomic clustering efforts. The class structure and model parameters are shown below:

Algorithm Dataset	Algorithm Name	Model Architecture	Resolution (um/px)	Minimum Object Size (um^2)	Classes
Rat Colon	ST_10X_Pub_RatColon_Anatomy_FF_r2_t1_all_v3_anno	DenseNet AI V2	1	500	Outer_Background, Outer_Muscular_Coat, Inner_Muscular_Coat, Myenteric_Plexus, Submucosa, Mucosa_Muscularis, Lamina_Propria, Crypt, Colonocyte_Border, Inner_Background

(Continued on next page)

Continued

Algorithm Dataset	Algorithm Name	Model Architecture	Resolution (um/px)	Minimum Object Size (um ²)	Classes
Rat Colon	ST_10X_RatColon_Tissue_Annotator_subset	MiniNet AI	5	2000	Background, Tissue
Rat Colon	ST_10X_RatColon_ConnectiveTissue_Annotator	MiniNet AI	5	2000	Background, Connective_Debris, Analyzed_Tissue
Mouse Syngeneics	ST_10X_Pub_Syngeneic_Tissue_Anno	MiniNet AI	5	2000	Background, Tissue
Mouse Syngeneics	ST_10X_Pub_Syngeneics_Tumor_Capsule_v2_anno	MiniNet AI	2.5	2000	Background, Tumor_Periphery, Tumor_Core
Mouse Syngeneics	ST_10X_Pub_Syngenic_B16_vs_MC38_v2	DenseNet AI V2	1	500	Background, MC38, B16
Mouse Syngeneics	ST_10X_Pub_Syngeneic_Melanin_v2_anno	MiniNet AI	1	200	Background, Tissue, Melanin
Mouse Syngeneics	ST_10X_Pub_Syngeneic_full_Necrosis_v2_anno	DenseNet AI V2	1	1500	Background, Tissue, Necrosis
Human PDAC-PolyA	ST_10X_Pub_PDAC_Tissue_Annotator	MiniNet AI	10	2000	Background, Tissue
Human PDAC-PolyA	ST_10X_Pub_FFPE_PDAC_EpiNonEpi_v5	MiniNet AI	1	500	NonEpithelium, Benign_Exocrine_Glands, Tumor, Background
Human PDAC-PolyA	ST_10X_Pub_FF_PDAC_EpiNonEpi_v3	MiniNet AI	2	100	Background, NonEpi1_smooth, NonEpi2_rough, Epithelium, Luminal_Space
Human PDAC-probes	10X_ST_Generic_FFPE_Blur_v1	MiniNet AI	1	1000	Background, Viable_Tissue, Blur_Tissue
Human PDAC-probes	ST_10X_2021_PDAC_TumorStromaExocrine_v3	DenseNet AI V2	1	200	Background, Stroma, Epithelium, Exocrine, White Space, Luminal Debris, Blood
All Studies	Nuclei Seg (Plugin) - BF v1.0.0	Nuclei Seg	-	-	Background, Nuclei

Once the list of classes was set, subsets of image areas were manually labeled in a semantic segmentation schema (e.g., pixel-level class labeling). All models were trained to minimize cross-entropy within annotated images. Once trained, the models were deployed across the entire tissue specimens to generate whole slide annotations with micron-level resolution.

A hierarchical approach was taken for model training and deployment (Figures 6I, S1A, S4F, S5F, and S7B). This enabled the semantic segmentation tasks to focus on inherently meaningful tissue while ignoring regions of background or artifactual pixels. As a result, the models required less training annotations for a given task.

Results of the trained models were reviewed for accuracy by a pathologist. When accuracy was confirmed, the resulting pixel-wise predictions were converted into polygon annotations and exported in an XML format for subsequent coupling with spatial transcriptomic data.

Nuclei were segmented across the whole-slide images using the HALO-AI Nuclei Seg classifier module. The Nuclei Seg model is based on a ResNet architecture¹²⁴ and was pretrained on standard hematoxylin and eosin-stained pathology slides. No updates were made to the model prior to deployment.

Digital pathology tissue co-registration

Whole slide images were co-registered using an automated elastic image registration tool (HALO, Indica Lab). Co-registration accuracy was reviewed and areas with visible mismatch between shared features were adjusted with addition of manual landmark annotations followed by re-processing of the co-registration algorithm.

Tissue identification and pathology integration

All sequencing outputs were processed using SpaceRanger-1.2.1 (10x Genomics) with rat (Rnor6.0ERCC-ensembl98), mouse (mm10-2020-A), and human (GRCh38-2020-A) references. Subsequent data processing and analysis were performed in R-4.0.3, Seurat-4.0.0¹¹¹ (which downsized original tissue images to approximately 600 by 600 pixels), and other R libraries

listed below. For each sample, spots were grouped into contiguous subclusters using `spdep-1.1-5`¹¹² and `igraph-1.2.6`¹¹³ libraries and 1.6-pixel distance to define contiguity. Subclusters of less than 100 spots were removed from the subsequent analysis.

Cell count and tissue compartment information (from the digital pathology analysis described above) were integrated using `spatstat-1.64-1`.¹¹⁴ A cell was assigned to a spot if the cell center was located within the area of the spot; then, all cell centers allocated to a spot were counted toward that spot (Methods). Tissue compartments were treated as polygons and assigned to spots based on the area intersection (Figures 2I, 3C, 3D, and 5B, S1G, S2A, S2B, S4G, S5G, S6A, and S6D). Then, tissue compartment information was summarized by *de novo* clusters (see details below; Figures 2J and 6J–6M, S1H, S2J, S2O, S4H, and S5H). In the BMS Spatial Portal Extended Pathology View (see details below), the compartment information was summarized by spot, i.e., each spot was assigned a single compartment that covered the highest percentage of the spot area. Tissue compartment information was used to filter spots. For rat colon samples, spots attributable to majority lumen and loose connective tissue were excluded. For syngeneic samples, spots not attributable to the tumor core were excluded. For pancreatic samples, spots attributable to tissue rips and pancreatic duct lumen were excluded. Digital pathology-defined tissue compartment information served to orthogonally validate transcriptomic-based annotations. This allowed for the high degree of confidence in such definitions needed for target discovery.

QUANTIFICATION AND STATISTICAL ANALYSIS

Promiscuous probe analysis

For the ST-FFPE-probes PDAC cohort (3 samples), we identified probes with low specificity by analyzing gene expression in spots outside of the tissue. If a gene was expressed in more than 95% of spots outside of the tissue, it was excluded from the analysis. A single gene was excluded from all three PDAC donor samples - SERF1A.

Pseudo-bulk expression analysis

For each tissue segment, we calculated expression pseudo-bulk counts defined as the total number of UMIs attributable to each gene across all spots within the tissue segment. In such pseudo-bulk analysis, each sample was represented by a single expression vector (Table S5). For each pair of samples, we compared their pseudo-bulk expression vectors by calculating the Pearson correlation coefficient and fitting a linear model (Figures 2D, 5C–5F, and 5H; S1K–S1N, S2D, S2E, S4D, S4E, S5D, S5E). Then, we performed the outlier analysis for each comparison by calculating residuals from the linear model and calling a gene an outlier if its absolute residual value was higher than the mean and three standard deviations of absolute values of all residuals (Table S5). To characterize the outlier genes for the PDAC Donor-A FFPE-poly vs FF-polyA comparison, we used STRING¹¹⁵ and manual curation (Figure 5G).

Expression comparison of co-registered PDAC samples

Two PDAC tissue sections from Donor-A-FFPE block were processed using ST-FFPE-polyA and ST-FFPE-probes protocols and their images co-registered (see description above). To compare the resulting gene expression profiles spatially, we identified pairs of spots most closely matching each other between two tissue sections according to their co-registered coordinates. We excluded any spot pair that was more than one spot diameter away from each other. Then, to account for any tissue shifts and RNA diffusion, we averaged the SCT-normalized gene expression in each spot with its nearest neighbors within 2 pixels (corresponding to the neighborhood of 16 spots total). We only included genes that were sufficiently expressed within both tissue sections, defined as expressed in at least 10 spots at 1 SCT-normalized expression or higher. We calculated Pearson correlation for all sufficiently expressed genes across successfully co-registered spots (Figure 5I).

Cohort integration and clustering

Samples were integrated using the CCA-approach implemented in the Seurat library¹²⁵ with 10,000 anchors and SCTransform normalization.¹²⁶ Optimal clustering resolution was selected manually with `clustree-0.4.3`¹¹⁶ library assisting in visualization.

Samples were integrated in the following groups:

1. rat colon samples 1 through 4 (as defined in the STAR Methods; Figures 2F, 2G and S1E)
2. rat colon samples 1 through 15 (as defined in the STAR Methods; Figures S1I and S1J)
3. B16F10 syngeneic samples (7 sections; Figures 3A and S2A)
4. MC38 syngeneic samples (6 sections; Figures 3B and S2B)
5. PDAC Donor-A ST-FF-polyA samples (4 sections; Figures 6A and S4A)
6. PDAC Donor-A ST-FFPE samples (6 sections; Figures 6B and S5A)

PDAC samples from Donor-B (Figure 6C) and Donor-C (Figure 6D) were treated as two independent cohorts due to the differences in the tissue composition across the three PDAC donors (described in the main text).

Spot cluster identity is visualized in the BMS Spatial Portal Extended Clusters View.

Marker gene identification and DEA

For each cohort, marker genes were identified using raw UMI counts using MAST¹¹⁷ through the FindAllMarkers function of Seurat (comparing each cluster to the rest of the spots) with the sample identity as a covariate. Resulting biomarkers were reported in Tables S2, S3, and S6 if they satisfied the following thresholds:

1. the percentage of cells where the gene is detected in the first group (pct_1) was at least 20%,
2. absolute value of the log2 fold change (avg_logFC) was at least 0.5,
3. and the negative log10 adjusted p value (p_val_adj_neg_log10) was at least 2.

Top biomarkers were visualized in the following dot plots: Figures 2H, 3E, 3F, and 6E–6H; Figures S1F, S2H, S2I, S4B, S4C, S5B, S5C, S6B, S6C, S6E, and S6F.

We performed additional differential expression analyses (DE-As) between the following groups of spots:

1. For syngeneic samples, pure B16F10 syngeneic spots compared to pure MC38 syngeneic spots (Table S3; Figure S2C),
2. For PDAC samples, tumor spots compared to non-tumor spots (Figures 7C and S7C; Table S7).

The specific definitions of these four groups follow.

Pure B16F10 and MC38 spots were defined as having 100% B16F10 and MC38 pathology compartment identity based on the digital pathology classifier (Figures S2A and S2B).

PDAC tumor spots were defined through the intersection of *de novo* clustering, digital pathology, and signature score analyses (Figures 7A, 7B, S7B, and S7C):

1. spots from *de novo* clusters 0 and 1 for Donor-A-FF, cluster 4 for Donor-A-FFPE, cluster 2 for Donor-B-FFPE, cluster 1 for Donor-C-FFPE,
2. spots with at least 50% epithelial content according to the digital pathology analysis,
3. spots with a significant Collisson classical PDAC signature⁸⁷ score (for details, see the next section).

Gene signature scores and P-Values

Gene expression signature scores were calculated using AddModuleScore¹²⁷ function from Seurat (Figures 2A–2C, 3I, 3J, 4C–4K, 5I, 6A–6D, and 7H; Figures S1B–S1D, S3A–S3I, and S7A). These are the values visualized in the BMS Spatial Portal Overview and Spatial Extended Views. For select signatures, we calculated empirical p values to assess the signature performance in each spot by drawing 10,000 random sets of genes of the same length as the signature and calculating corresponding gene scores. We called a signature score significant if it was higher than at least 9,995 bootstrapped scores, corresponding to the empirical p value of 0.0005.

Tumor depth modeling for syngeneics samples

For each syngeneic tissue section, we calculated the distance from the tumor edge to the tumor center using the digital pathology definition of the tissue edge and the spatstat-1.64-1 library.¹¹⁴ The resulting pixel distances were transformed to a percent relative to the maximum distance within each tissue section to normalize for the size of the tumor. We ignored any tissue rips and necrotic areas within the tumor.

For B16F10 and MC38 cohorts independently, we selected highly expressed genes defined as genes expressed in at least 100 spots at 0.5 SCT-normalized level or higher. Then, for each gene in each of the two cohorts, we fit a linear model with the following formula: gene expression by spot \sim spot distance to center (%) + number of cells per spot. We collected the p value and the effect size of the distance coefficient of each model, and we called a gene significantly associated with the tumor depth if:

1. its p value was less than 0.05 after Bonferroni correction for the number of genes tested within each cohort,¹²⁸
2. its effect size was higher than then mean and three standard deviations of the absolute values of the effect sizes of the cohort (Figures 4 and S3; Table S4).

Receptor-ligand pair analysis

We downloaded the FANTOM5 database^{33,54,92,129} of previously identified receptor-ligand pairs and selected those gene pairs that were sufficiently expressed in our data, defined as expressed in at least 5 spots at 1 SCT-normalized level or higher. For each gene pair in the database, we identified their scaled and SCT-normalized expression profiles in our PDAC ST-FFPE-probes data. For each of the three PDAC samples, we calculated spot-by-spot Pearson correlation and mutual information for each of the receptor-ligand pair (Table S7). If the gene pair correlation coefficient or the mutual information value was higher than the average and the two standard deviations of the respective metric for all gene pairs considered for a sample, we called that gene pair as putatively interacting. This is a similar method to those published previously.^{33,54,129} For visualization purposes, if the gene expression in a spot was more than 0, it was considered expressed in that spot (Figures 7D–7G).

ADDITIONAL RESOURCES

BMS spatial portal

The BMS Spatial Portal is an R-Shiny application implemented using open-source infrastructure including *periscope*¹¹⁸ and *canvasXpress*¹¹⁹ that visualizes spatial distributions of gene expression from Visium technology. It can be accessed at the following link: http://periscopeapps.org:3838/spatial_portal/. The code and the data from the portal were released on GitHub under a GNU General Public v3 license. Due to data size constraints, the Portal contains 8 representative samples from the cohorts we describe above while the rest of the data can be found on GEO. To improve Portal performance input Seurat objects were stripped of auxiliary information using the Seurat library *DietSeurat* function.¹¹¹ Samples included in the portal are listed in the Methods.

For each individual sample, the portal spatially plots SCTransform-normalized expression values of individual genes or gene signature scores (calculated as described above). The signatures included in the Portal are summarized in [Table S1](#).^{27–62} The Extended View of the Portal adds spatial views of *de novo* clustering and pathology compartments (described above), as well as the H&E tissue image. For gene signatures, the Extended View of the Portal also provides a dot-plot of individual gene expression values summarized by *de novo* clusters. For individual genes, the Extended View of the Portal provides a bar-plot of the gene expression summarized by *de novo* clusters.